Journal of Electroanalytical Chemistry 1007 (2026) 119883

Contents lists available at ScienceDirect

Journal of Electroanalytical Chemistry

journal homepage: www.elsevier.com/locate/jelechem

Correlation of the role of Li-doping in control of O-vacancies and Li-interstitial formations in NiO with electrochemical properties

Poonam Singh [a], P. Maneesha [a], Manju Kumari [a], Abdelkrim Mekki [b,c], Khalil Harrabi [b,d], Somaditya Sen [a,*]

[a] *Department of Physics, Indian Institute of Technology Indore, Indore 453552, India*
[b] *Department of Physics, college of engineering and physics, King Fahd University of Petroleum and Minerals, Dhahran 31261, Saudi Arabia*
[c] *Center for Advanced Material, King Fahd University of Petroleum & Minerals, Dhahran 31261, Saudi Arabia*
[d] *Interdisciplinary Research Center for Advanced Quantum Computing, King Fahd University of Petroleum and Minerals (KFUPM), Dhahran 31261, Saudi Arabia*

ARTICLE INFO

Keywords:
Oxygen vacancy
Li interstitials
Strain and disorder
Structure correlated physical properties
Conduction properties
Electrochemical properties

ABSTRACT

Monovalent doping in a divalent cationic oxide material like NiO introduces modifications in the cationic valence state of the lattice and differences in the ionic radii of the cationic site. Such modifications introduce changes in the oxygen lattice and can introduce interstitial cationic sites, thereby increasing the strain and disorder in the lattice and modifying the bond lengths, leading to changes in the electronic, transport, and capacitive properties, which results in modifications in the charge storage properties. Monovalent Li^+ doping in NiO is commonly noticed in literature. However, an attempt to correlate the defect formation and associated changes in structural, vibrational, and electronic properties and thereby correlate these to the charge storage properties has not been made. In a first-of-its-kind report, this work reveals that the charge storage properties improve until 3% Li^+ substitution and thereafter decrease for 6%. The defect study of these materials hints at Li-interstitial being the responsible factor behind such degradation. The connection of oxygen defects, and Ni^{2+} to Ni^{3+} transformation seems to increase the charge storage.

1. Introduction

Capacitive electrode materials facilitate high power density, rapid charging, and long cycle life, making them important as energy storage materials [1,2]. Nickel oxide (NiO) is well-known for such properties and possesses good thermal and high chemical stability [3]. It is naturally abundant, and environmentally friendly [3]. On top of that it is not expensive [3]. However, in spite of a high theoretical specific capacitance of 2584 F g^{-1} in potential window of 0.5 *V* [3], NiO shows a low experimental value of specific capacitance (C_S), due to its low conductivity (resistivity $\sim 10^{13}\,\Omega$ cm) [3,4]. Hence, attempts have been made to dope NiO by various elements to improve the conductivity of the material [4–7]. By modifying the surface area with different types of morphologies [3,4,8], attempts have been made to improve C_S [8].

Among all possible dopants, monovalent cation doping is an interesting problem as it is supposed to introduce oxygen defects or interstitial cations [4]. Among all the monovalent cations the Li^+ ion (0.9 Å) is the closest in size to the host Ni^{2+} ion (0.83 Å) [9]. Hence, exploration of different amount of doping without creating a massive lattice strain and disorder is of primary interest. Li^+ incorporation in NiO leads to several possibilities: $Ni^{2+} \rightarrow Ni^{3+}$ transformation, creation of oxygen defects (O_V), and creation of Li^+ interstitial (Li_i) [4]. Such changes in the lattice modify the ligands field and hence the bonds. As a result, the electronic properties, and therefore the transport, and charge storage properties are modified [4–7]. Also to mention, the literature is flooded with abnormally high percentage of doping ($\geq 6\% \sim 50\%$) which seems to be unrealistic because of the differences of the ionic radii, valence state, increasing lattice strain, and defect formation possibilities [4–6,10,14–22]. There are reports with lower percentage doping ($\leq 3\%$) which seem more realistic [11–13,23–25], but these too fail to correlate lattice structural changes to the changes in the opto-electronic, transport, and hence charge storage properties.

In this study, Li^+ doping in NiO has been explored, investigating the dynamics of defect formation like oxygen defects, $Ni^{2+} \rightarrow Ni^{3+}$ conversion, and Li_i formation. Further, these factors have been correlated to the structural, vibrational changes to the electronic, transport, and hence the charge storage properties. In the process an optimization of the amount of Li^+ doping has been obtained for maximum charge

---

* Corresponding author.
E-mail address: sens@iiti.ac.in (S. Sen).

https://doi.org/10.1016/j.jelechem.2026.119883
Received 10 October 2025; Received in revised form 6 January 2026; Accepted 27 January 2026

storage properties.

2. Experimental procedure

$Ni_{(1-x)}Li_{(x)}O$ nanocrystalline powders were synthesized using the following precursors: nickel (II) nitrate hexahydrate ($Ni(NO_3)_2.6H_2O$, 99%, Alfa Aesar) and lithium(I) nitrate ($LiNO_3.9H_2O$, 99%, Alfa Aesar). Calculated amount of the above chemicals was taken in separate beakers and dissolved in de-ionized water (DIW). After obtaining homogeneous solutions, the lithium solution was added to the nickel solution. The mixtures were stirred for two hours to ensure the homogenous mixing of the two precursors. In another beaker a calculated amount of citric acid and ethylene glycol were mixed thoroughly in DIW. The clear citric acid and ethylene glycol solution was added to the precursor solution to act as monomer and thereafter polymer formation upon uniformly heating at 80 °C on a hot plate required for gel-formation. This polymer network later on acted as a fuel during burning of the gel at the same temperature. The obtained powders were then dried and decarbonized and denitrification at 450 °C. Further, these powders were heated at 600 °C to finally obtain fluffy black powders containing nanoparticles of $Ni_{(1-x)}Li_{(x)}O$. The samples were named S0 (for $x = 0$), S1 ($x = 0.016$), S3 ($x = 0.031$), and S6 ($x = 0.062$) [Fig. 1].

The structural phase of these samples was confirmed using a Bruker D2 Phaser diffractometer equipped with Cu-K_α radiation ($\lambda = 1.54$ Å). For X-ray photoelectron spectroscopy (XPS) measurements using Thermo-Scientific Escalab *250* Xi, monochromatic Al K_α X-rays ($h\nu = 1486.6$ *eV*, $\lambda = 8.3$ Å) operating at *150 W* under ultra-high vacuum ($\sim 10^{-9}$ mbar) were employed. A survey spectrum was initially obtained for each sample in the binding energy range of *0–1400* eV. Thereafter, high-resolution Ni2p (*840–890* eV), Li1s (*46–62* eV), and O1s (*520–540* eV) spectra were obtained. The spectra were analyzed with the help of XPSPEAK4.1 software. Liquid-state Fourier-Transform Nuclear Magnetic Resonance (FT-NMR) measurements were carried out using a Bruker AVANCE III 400 Ascend FT-NMR spectrometer (Bruker BioSpin International AG, Switzerland). The surface morphology of the samples was studied using a Carl Zeiss FESEM/EDS-Supra55 microscope. The chemical compositions of the samples were analyzed using an inductively coupled plasma–optical emission spectrometer (ICP-OES) (Agilent 5800, Agilent Technologies, USA) after appropriate acid (HNO_3) digestion. The vibrational properties, i.e., the phonons were studied using a LabRAM HR Evolution (Horiba) Raman spectrometer. A He—Ne laser of wavelength *632.8* nm was employed for excitation. The electronic band gap was obtained from the UV–Vis diffuse reflectance spectra (DRS) using a Perkin Elmer Lambda *35* UV–Visible spectrophotometer. A Teflon (polytetrafluoroethylene, or PTFE) sample was used as a reference material for perfect reflection. Specific surface area and pore characteristics were determined from nitrogen adsorption–desorption isotherms recorded at 77 K using a surface area and porosity analyzer (Autosorb iQ^2, Quantachrome Instruments, Anton Paar, USA). 180 °C degassing temperature was employed for 2 h to all the samples, before the adsorption experiments. The Barret–Joyner–Halenda (BJH) method was used to analyze the pore size distribution.

Cyclic voltammetry (CV) measurements were carried out using an electrochemical workstation (make: Kanopy). An Ag/AgCl (*3* M KCl) reference electrode was used with platinum wire as the counter electrode. Ni foams (NFs) (Sigma-Aldrich: thickness of *2* mm, bulk density of *0.45* g cm^{-1}, porosity of *95%, 20* pores/cm, and purity of *99.5%*) were used as the working electrodes onto which the active material was deposited by drop-casting a dispersed solution containing the materials. The NFs were cut into strips of dimension *2* cm × *1* cm. An optimization was performed on the effect of the etching of NFs. It was observed that a short time etching (≤ 1 min) with a low HCl concentration (≤ 0.1 M) is best suited for removing contamination and increasing the surface roughness thereby improving the adhesion between substrate and active material. For a more concentrated HCl solution (> 0.1 M) and longer etching time (> 1 min) an oxide layer seemed to form on the NFs. This can lead to additional NiO layers of different properties. Hence such conditions were avoided by sonicating the NFs in *0.1* M HCl for only *1* min for this study. These etched NF pieces were thereafter cleaned with ethanol. Note that the area of the CV spectra increased for etched NF as compared to the commercial and only ethanol cleaned NFs

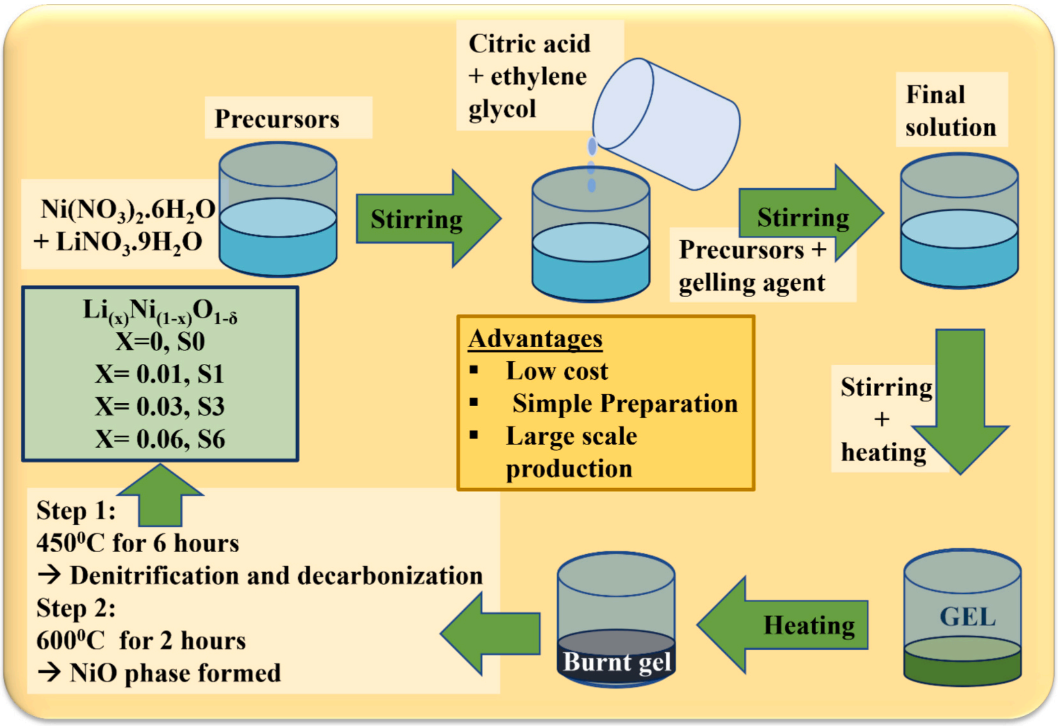

Fig. 1. Representation of the synthesis process of Li-doped Ni via sol-gel synthesis route.

[Supplementary Fig. S1 (a)]. The Li-doped NiO samples were deposited on these cleaned NF substrates for electrochemical performance. Mixers of active material (Li-doped NiO) with acetylene black, and Nafion in a weight ratio of *80:10:10* in *500* μL of ethanol were prepared. The combination was ultrasonically mixed for one hour to obtain dispersed solutions with different concentrations. The dispersed solutions were carefully drop-casted on the NFs with different mass loading: *2* mg, *3* mg, *4* mg, *5* mg, and *6* mg such that the entire NF gets evenly coated. These coated foams were left to dry in an oven overnight at *80 °C* [Fig. 2]. After drying overnight at *80* °*C*, the coated NFs were ready for CV, Galvanostatic Charge-Discharge (GCD), and electrochemical impedance spectroscopy (EIS) studies. Among the different concentrations of the active materials, the CV spectra revealed a maximum enclosed area for the *4* mg sample implying the maximum C_s for this sample at 10 mV/s [Supplementary Fig. S1 (b)]. Therefore, *4* mg mass loading will be used as a benchmark for further discussions. Hence, in this work electrochemical studies will be performed on 4 mg mass loaded samples of doped and un-doped NiO deposited on a *0.1* M HCl etched (*1* min) NF. These samples will be hereafter referred as eNF (bare etched NF), S0/NF (NF coated with S0), S1/NF (NF coated with S1), S3/NF (NF coated with S3), and S6/NF (NF coated with S6). The CV spectra was recorded at 50 mV/s for the pristine, 0.1 M HCl-treated (1 min), S0, and S3 samples (with comparable mass loading of ~4 mg). The spectra revealed clear differences in electrochemical behavior of the samples [Supplementary Fig. S1 (c)]. The adhesive stability of the coats was verified by FE-SEM of the cross-section of the materials deposited on the NF, before performing CV and GCD. EIS was recorded in the frequency range from *100* kHz to *0.01* Hz using a *5* mV AC perturbation. The electrochemical properties (CV and GCD) were studied using a three-electrode assembly cell with a *6* M KOH electrolyte within a positive potential window. Cyclic Stability tests were performed using GCD at two fixed current densities of 5 and 10 A g^{-1} for 1000 continuous cycles.

3. Results and discussion

3.1. X-ray diffraction (XRD) analysis

The XRD patterns of the Li-doped NiO nanocrystalline powders revealed diffraction peaks corresponding to $Fm-3m$ structure (COD #1010093) [Fig. 3 (a)] [26]. Rietveld refinement [Fig. 3 (b), Supplementary Fig. S2] revealed a decrease in lattice parameters for Li-doped samples compared to pure NiO. With Li-incorporation, the lattice parameters decreased from 4.17 Å (S0) to 4.169 Å (S1) and 4.168 Å (S3) [4,22], and thereafter slightly increased to 4.17 Å (S6) [Fig. 3 (c)] [4,12,13]. The unit cell volume decreased accordingly from 72.512 $Å^3$ (S0) to 72.459 $Å^3$ (S1) and 72.407 $Å^3$ (S3) [22], and thereafter slightly increased to 72.511 $Å^3$ (S6) [4,13,22]. In NiO, the oxidation state of Ni is supposed to be in the Ni^{2+} state with coordination six. The ionic radius of Ni^{2+}(VI) ion is 0.83 Å [9,13]. With the incorporation of Li^{+}, one can envisage several scenarios involving different vacancies, interstitials, valence states, etc. [4,5]. However, the most important and natural consequence of the presence of a lower valence Li^{+} in place of a higher valence state Ni^{2+} is expected to create O_v. Hence, this may lead to a lattice containing Ni^{2+}, Li^{+}, O^{2-} and O_v according to the following possibility [4,6,13]:

$$(x)\ Li^{+} + (1-x)\ Ni^{2+} + O \rightarrow Ni^{2+}_{(1-x)} Li^{+}_{(x)} O_{(1-x/2)}\ O_{v(x/2)} \tag{1}$$

However, the presence of Li^{+} can also induce a transformation of the valence state from Ni^{2+} to Ni^{3+}, thereby reducing the total O_v content [6,11,13,21,22,25]:

$$(x)\ Li^{+} + (y)\ Ni^{3+} + (1-x-y)\ Ni^{2+}\ O \rightarrow Ni^{2+}_{(1-x-y)}\ Ni^{3+}_{(y)}\ Li^{+}_{(x)}\ O_{(1-(x-y)/2)}\ O_{v(x-y)/2} \tag{2}$$

Such possibilities can only be verified by studying the valence states of the constituent elements using probes like XPS. Note that the Ni^{3+}(VI) ion is much smaller ~0.6 Å (high spin, HS) or ~ 0.56 Å (low spin, LS) than the Ni^{2+} ion, while the Li^{+}(VI) ion is much larger (0.9 Å) than both oxidation states of Ni ions [9,13]. A simple substitution of Ni^{2+} by Li^{+} should expand the lattice. This is contradictory to the unit cell volume contraction in S1 and S3 [4,13], which may be a consequence of O_v and Ni^{3+} formation [4,13]. In the case of S6, the volume expansion can be a consequence of some Li^{+} ions occupying interstitial positions which requires extra space in the lattice [4,13]. To verify and substantiate these claims XPS analysis becomes an important study in this work. Such inclusion of O_v, Li_i, and Ni^{3+} ions are consequences of Li doping and may result in the deformation or irregularity of the lattice, thereby increasing the lattice strain and disorder. The microstructural strain (ε) and crystallite size (D) were estimated using the Williamson–Hall (WH) Eq. [24]: [$\beta.\mathrm{Cos}\theta = \varepsilon.4\mathrm{Sin}\theta + K\lambda/D$; a "$y = mx+c$" format where $y = \beta.\mathrm{Cos}\theta$, $x = \mathrm{Sin}\theta$, $m = \varepsilon$, and $c = K\lambda/D$], where, β is full width at half maxima (FWHM), θ is angle of incidence of X-ray, λ is wavelength of X-ray (*1.5406 Å*), and K (~ *0.94*) is a constant dependent on morphology. The ε was observed to increase with substitution from 0.00173 in S0 to 0.00175 in S1, 0.0018 in S3 and 0.00199 for S6 [Fig. 3 (d)] [11,12]. Note that this continuous increase of strain indicates the effect of the

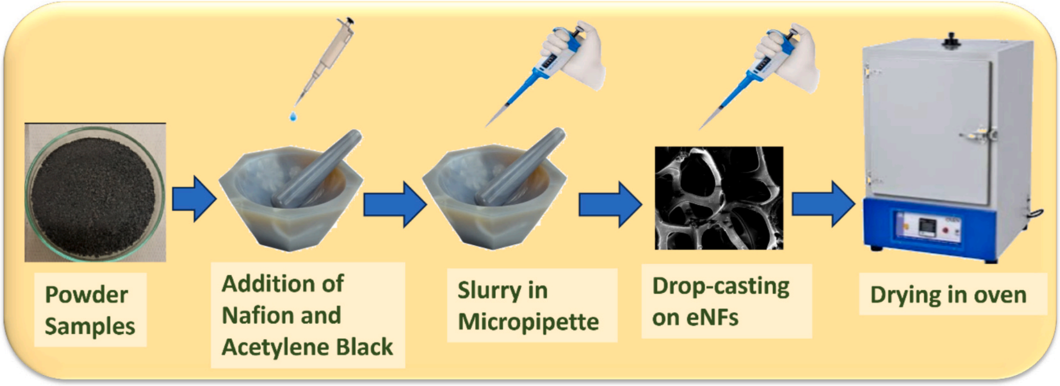

Fig. 2. Representation for the working electrode preparation via drop casting method on NFs.

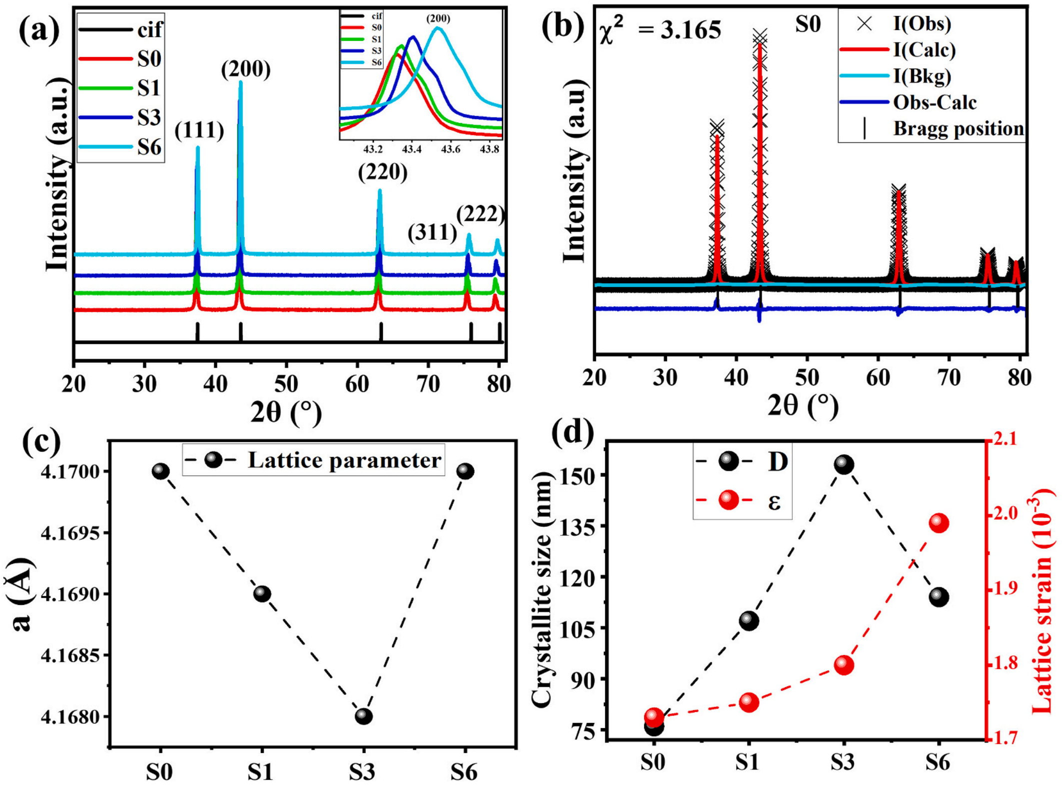

Fig. 3. (a) XRD pattern of all samples revealing a Fm-3 m space group consistent with COD #1010093, (a–i) magnified image of (200) peak showing shift with doping revealing changes in the lattice parameters, (b) a representative representation of a Rietveld-refinement of the pure NiO sample revealing good fitting, (c) Variation of lattice parameters with substitution, (d) variation of crystallite size and strain with substitution calculated from Williamson–Hall (WH) formula.

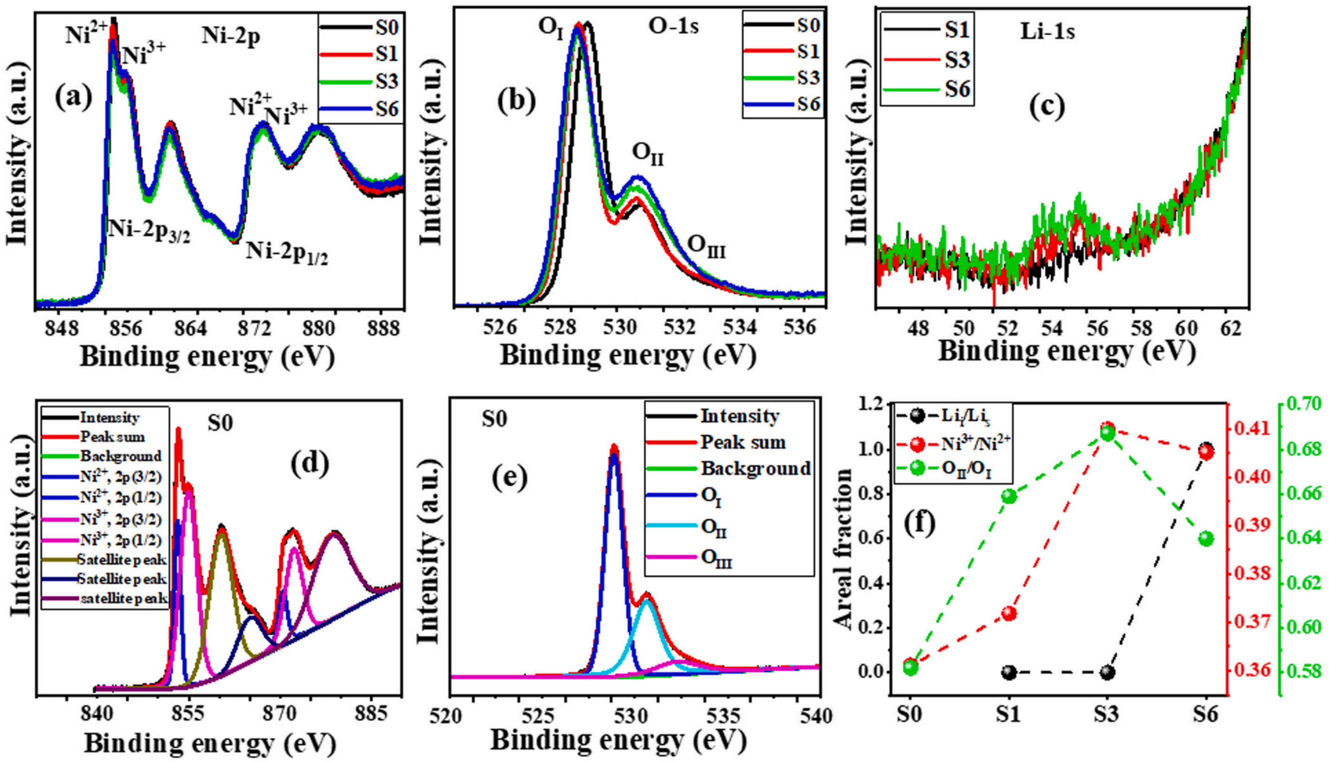

Fig. 4. (a) Ni-2p XPS spectra for all the samples revealing changes in the different components of the spectra, (b) O-1 s XPS spectra for all the samples revealing modifications with doping, (c) a weak Li-1 s XPS spectra revealing an increase of Li content with doping for all samples, 3(d and e) representative fitting of of Ni-2p and O-1 s XPS spectra of pure NiO revealing contributions from Ni^{2+} and Ni^{3+} components with different spin contribution and three different components of the oxygen spectra corresponding to lattice, adsorbed oxygen, and water adsorption, respectively, (f) Variation of the Ni^{3+}/Ni^{2+} peak area fraction with.

larger Li^+ ion in the lattice is associated with a consequential introduction of Ni^{3+}, O_v, and Li_i. However, D increased from S0 (76 nm) to S1 (107 nm), and S3 (153 nm) [4,11], and thereafter decreased for the S6 sample (114 nm) [11,12]. Hence, the crystallites were large enough for the chemically modified samples to be called nanoparticles. However, from the nature of the peaks and the FWHM [Supplementary Fig. S3], the crystallinity increased for S1 and S3 samples with the increase of size of the crystallites [10,11], which decreased for the S6 sample, may be due to an interstitial nature of Li, which increased the strain further [11]. Note that the XRD data has a very clean non-amorphous background thereby revealing perfect crystallinity of the materials despite the increasing strain in the lattice with doping [10].

3.2. X-ray photoelectron spectroscopy (XPS) analysis

The Ni-2p, O-1 s, and Li-1 s XPS spectra were explored to confirm the valence states of the elements of the synthesized samples at room temperature. For the pure NiO sample, the Ni-2p spectra revealed a convoluted feature of seven peaks, belonging to Ni^{2+}-$2p_{3/2}$ (~ 853.15 eV), Ni^{3+}-$2p_{3/2}$ (~ 854.94 eV), Ni^{2+}-$2p_{1/2}$ (~ 870.45 eV), Ni^{3+}-$2p_{1/2}$ (~ 872.24 eV), with three satellite features (at ~860.29 eV, ~ 865.01 eV, and ~ 878.42 eV) [Fig. 4 (a, d), Supplementary Fig. S4] [6,10,13,25]. Hence, the spin-orbit splitting (SOS) energy between the Ni^{2+}-$2p_{3/2}$ and Ni^{2+}-$2p_{1/2}$ states was observed to be ~17.3 eV. A similar SOS ~17.3 eV between the Ni^{3+}-$2p_{3/2}$ and Ni^{3+}-$2p_{1/2}$ states was also observed. Note that a standard value of the Ni-SOS is ~17.49 eV [10] which is close but higher than the SOS of S0 ~ 17.3 eV. A slight shift towards lower binding energy was observed in both Ni-$2p_{3/2}$ and Ni-$2p_{1/2}$ peaks with Li doping, which indicated that the electron density around the Ni cations was reduced [25]. Note that, SOS for both Ni^{3+}-$2p_{3/2}$ and Ni^{3+}-$2p_{1/2}$ and Ni^{3+}-$2p_{3/2}$ and Ni^{3+}-$2p_{1/2}$ were maintained at ~17.3 eV. With an increase of Li content an increase of the Ni^{3+} content was estimated from the ratio of the Ni^{3+}/Ni^{2+} peak areas [Fig. 4 (f)]. The fraction was observed to increase from 0.361 (S0), 0.372 (S1) to 0.41 (S3) [13,25], and thereafter nominally reduce to 0.405 (S6) [25]. This hinted at $Ni^{2+} \rightarrow Ni^{3+}$ conversion with Li doping until S3 with a slight reduction for S6 [13].

The O-1 s core-level spectrum of NiO [Fig. 4 (b, e), Supplementary Fig. S5] exhibited a dominant asymmetric peak centered at 528.87 eV (denoted as O_I), characteristic of lattice oxygen in the Ni—O (Ni^{2+}-O^{2-}) framework [6,10,13,25]. A pronounced shoulder at 530.62 eV (denoted as O_{II}) is attributed to defect-related oxygen species [10,13,25]. A weaker high–binding-energy component at 532.32 eV (denoted as O_{III}) is assigned to physiosorbed water and carbonate species. This O_{III} contribution is default to the samples due to the ambient exposure prior to measurement and is not a subject of this study [10,13,25]. In the pristine NiO (S0), O_I dominated the spectrum, indicating a predominantly Ni^{2+}-O^{2-} environment. With progressive Li doping (S1, and S3), the relative intensity of O_{II} increased at the expense of O_I [10,13,25]. Quantitative peak area analysis of the O_{II}/O_I peak area ratios revealed an increase with an increasing Li content until S3 and then reduced for S6 [Fig. 4(f)] revealing a similarity with the Ni^{3+}/Ni^{2+} ratio [10,13]. This similarity hints at a correlation of the increase of oxygen defect species with an increase of Ni^{3+} content as a consequence of the charge compensation in the lattice due to lesser valent Li^+ substitution of Ni^{2+} [13]. Such changes are supposed to introduce additional electronic states that can enhance surface reactivity [13].

However, due to the low photoionization cross-section of Li and surface sensitivity of XPS, direct and reliable detection of Li, especially at low doping levels, is challenging [10]. It can be observed that Li-1 s revealed a weak broad and noisy feature at ~55 eV belonging to substitutional Li (Li_s) for S1 sample, which became more prominent for the S3 and S6 samples [10]. However, along with the Li_s peak an additional Li_i (~53.8 eV) peak was observed for the S6 sample with the maximum Li content. Note that the Li_s and Li_i were convoluted [Fig. 4 (c), Supplementary Fig. S6] [27]. Li_i typically shows a lower binding energy compared to Li_s, reflecting a more "metallic" or less bound state [28]. Notably, in S6, Li_i:Li_s was found to be ~1:1, which indicates that almost 50% of the Li in the lattice is Li_i. Hence, XPS studies provided an important information that the solubility limit of Li in the NiO lattice is ~3%, and beyond 3% Li_i will be introduced in the lattice due to the larger size of the Li^+ ion [Fig. 4(f)] [13].

Note that the XRD studies revealed similar changes showing reduction of unit cell volume, and increase in the crystallite size until S3 thereafter reversing the trend for S6. Hence, the solubility of the Li in the lattice seems to be responsible for the reduction of cell volume due to a probable increase of Ni^{3+} and O_v. On the other hand, beyond the solubility limit, the advent of Li_i in S6, there is a reduction of Ni^{3+} and O_v [Fig. 4 (f)]. Hence XPS and XRD are commensurate with each other.

To complement the XPS analysis and probe Li incorporation more sensitively, ^7Li nuclear magnetic resonance (NMR) spectroscopy was performed after dissolving the samples in D_2O [Fig. 5] [29]. No Li resonance was observed for the pristine sample (S0), confirming the absence of Li [29]. A distinct ^7Li resonance centered at ~0.141 ppm in the NMR spectra provided a direct evidence for Li incorporation in all the Li-doped samples [29]. Apart from this main peak, a shoulder peak at a slightly higher ppm was observed for S1 and more prominently for S6, but was missing for S3 [29]. Note that shoulder peaks are associated with several contributions, including defects due to Li [29] and also due to interactions of Li^+ with Ni^{2+} and Ni^{3+} ions via intermediate O ions [29]. As discussed in the previous sections, Li-incorporation may lead to formation of Ni^{3+}, O_v, and Li_i, making possible many interactions which were absent in the pure NiO [29]. Such a dynamic set of conditions can be responsible for the shoulder peaks to appear in the NMR spectra of S1 and S6. For any solid solution, there are certain parameters where the lattice becomes unique for a certain performance. Such "Goldilocks zone" represents a desirable target which satisfies a precise set of conditions where competing constraints are balanced to achieve optimal performance [30]. In S3, such a situation may be obtained for Li-accommodation. However, this is merely a speculation, not a claim as the present ^7Li NMR measurements were performed in the liquid state after dissolving the samples in D_2O. In the liquid-state NMR, the spectra reflect an average local chemical environment of Li rather than crystallographically resolved site occupancy in the solid lattice [29]. Further, ^7Li NMR does not directly probe O_v. Instead, it is sensitive to vacancy-induced modifications in the local electronic and ionic environment surrounding Li ions [29]. Therefore, features such as peak broadening or shoulder-like asymmetry are interpreted as indicative of multiple Li environments or local disorder, rather than definitive evidence for specific defect configurations such as Li_i. Accordingly, the combined XPS–NMR analysis provides indirect but consistent evidence supporting the defect-related interpretations presented in this work.

3.3. FESEM and EDS

FESEM studies were performed to investigate the surface morphology of the samples [Fig. 6]. The effect of Li^+ on the particle size and morphology is important to understand the charge storage properties. FESEM images of the doped samples revealed that the morphology remained more or less the same, with agglomerated spherical nanoparticles forming the building block of the material. The agglomerations seemed to be a collection of smaller nanoparticles forming larger particles that are further agglomerated to form the building block of the materials. This gave the morphology a granular and porous nature [11,13,23].

The elemental composition obtained from EDS measurements for all the samples revealed signatures of Ni and O only without the detection of the presence of Li. Li has a very low atomic number ($N = 3$), with a Li Kα X-ray energy ≈ of approximately 54 eV. This is far below the detection window of conventional Si (Li) or SDD EDX detectors, as well as the transmission threshold of detector windows (even those labeled as "ultrathin" or polymer windows). The low energy of the Li X-rays is

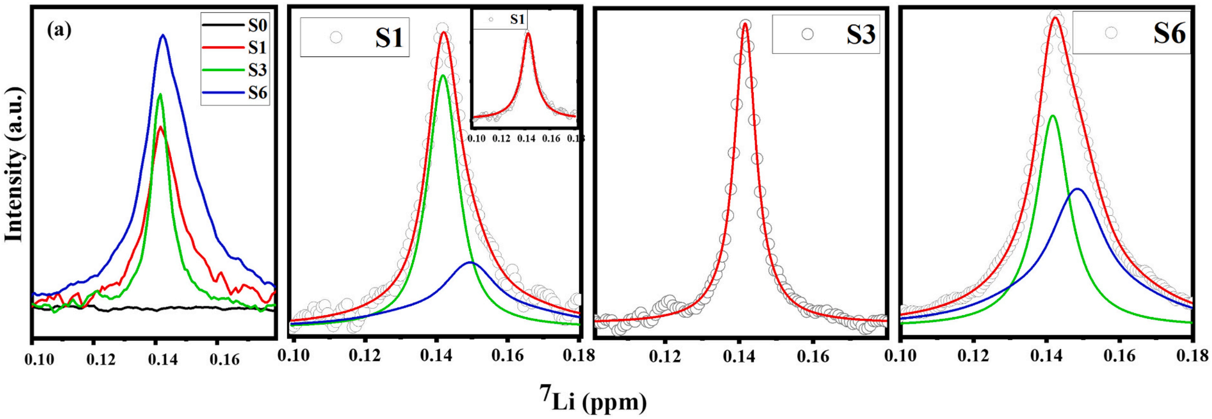

Fig. 5. Liquid-state ^{7}Li NMR spectra recorded after dissolving the samples in D₂O: (a) comparison of pristine (S0) and Li-doped NiO samples (S1, S3, and S6) exhibit a ^{7}Li resonance centered at ~0.141 ppm, confirming the presence of lithium. The deconvolution in (b–d) reveals multiple spectral components, indicating the coexistence of different lithium environments in the doped NiO samples. The inset in Fig. 5(b) shows the spectrum of S1 fitted with a single component, illustrating the poor fit quality.

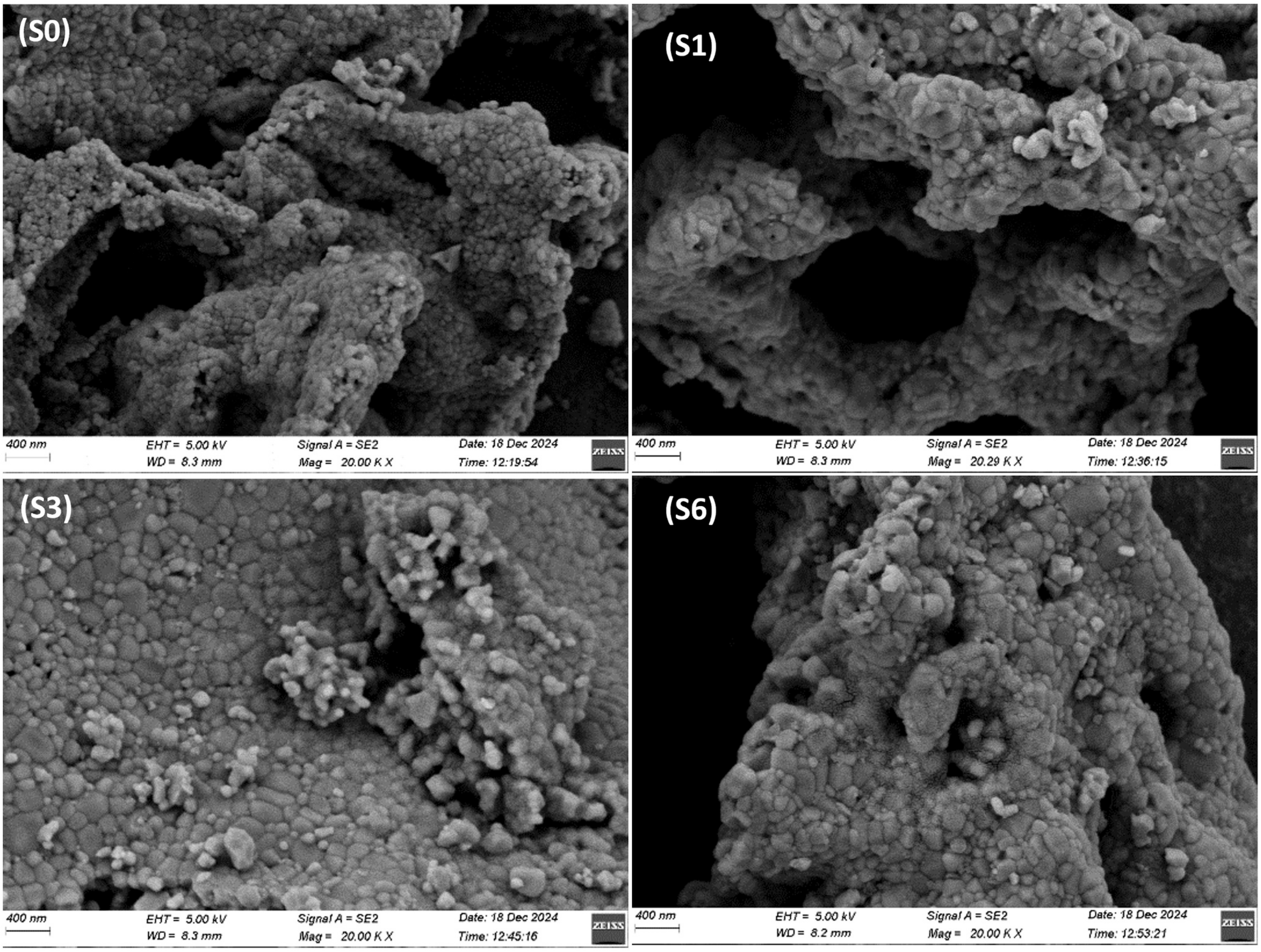

Fig. 6. FESEM images of Li-doped NiO samples revealing agglomerated nanoparticles with 20 k magnification.

absorbed even before they reach the detector. Hence, using EDX (EDS) the detection of Li even in S6 with highest ~6% Li-doping is extremely challenging under standard conditions and therefore was not observed. The Ni:O ratio in all the samples are in the acceptable range confirming the stoichiometry of the samples to be of the same structure as NiO [31].

To overcome the EDX limitation and obtain quantitative information on Li content in the samples, ICP-OES (Inductively Coupled Plasma - Optical Emission Spectrometry) was performed on the samples [Supplementary Table S7] [22]. ICP–OES offers improved sensitivity for lighter elements compared to EDX and enables bulk compositional analysis. Equal amounts of each sample were dissolved in a calculated amount of HNO_3, while maintaining identical synthesis conditions across all samples. However, Li was detectable only for the higher-doped samples [22]. While the quantity was calculable for S6 (0.00016 mg/L), the value was low enough to be calculable for S3, and was not observed for S1 [22] as for lower doping levels, the Li concentration approached the detection limit of the technique, making it difficult to establish a clear monotonic trend across the series [22]. Hence, after not being able to estimate Li for all the samples and ensure the presence of Li in the samples, it was understood that NMR was the only powerful tool to detect Li [29]. As discussed before, the presence of Li was proved from ^{7}Li NMR spectra [Fig. 5] [29].

3.4. UV–visible diffuse reflectance spectra analysis

The band gap, E_g, was estimated from the reflectance percentage ($R\%$) obtained from UV–Vis Diffuse Reflectance Spectra (UV–Vis DRS) in the wavelength regime 200–1100 nm [10]. Thick non-transparent samples were used to reduce the transmission coefficient to zero, allowing only the possibilities of absorbance ($A\%$) and reflectance ($R\%$). The Kubelka-Munk function, $F(R)$ was used to calculate the equivalent absorption coefficient (α), $\alpha \cong F(R) = (1-R)^2/2R$, where R ($=R\%/100$) is the diffuse reflectivity [10]. Using the Tauc method, the optical band gap was computed using energy-dependent optical absorbance data [10]. The Tauc method involves a relationship between α, photon energy (E) $= h\upsilon$, and E_g in the form [6,10]: $(\alpha h\upsilon)^{1/n} = A(h\upsilon - E_g)$; where α is the absorption coefficient, υ is the photon's frequency, h is Planck's constant, A is a proportionality constant, and E_g is the band gap. For a direct allowed bandgap, $n = ½$ [6,10]. Hence, a Tauc plot of $(\alpha h\upsilon)^2$ vs $h\upsilon$ was plotted for all samples [Fig. 7 (a)]. The optical E_g was determined by protraction of the linear parts of this plot to the x-axis [$(\alpha h\upsilon)^2 = 0$] [5,6,11]. The spectra of all samples exhibited one main absorption peak. However, multiple distinct pre-absorption features were observed for S0 and S1 [32]. The main absorption edge resulting in the energy gap, E_g (band gap) was due to an O2p to Ni3d transition. E_g was observed to decrease with Li^+ doping from 3.86 eV in S0 to 3.85 eV in S1 and 3.84 eV in S3 [Fig. 7 (b)] but increased to 3.89 eV in S6 [5,11,12]. These changes were visually observed from Tauc plots. However, as observed from their values the changes were minimal. Hence, not much significant claim could be made from these changes. With Li^+ doping an increase in the concentration of free charge carriers could be expected with the incorporation of lattice defects created due to a mismatch of the valence state and the ionic radii of the dopant and the host [Supplementary Fig. S8] [4–6,10,11]. Some reports used Hall effect measurement to reveal the increase of carrier concentration with Li-doping [5,20]. Hence, the visual differences in the primary absorption edge may be real.

The multiple distinct pre-absorption features in the visible spectra can be assigned to distinct absorption peaks originating from optical transitions between different energy levels of the d orbitals of Ni^{2+} ions. A Ni^{2+} ion in NiO has an electronic configuration of $3d^8$, in an octahedral field. In the crystal-field (CF) framework, the Hamiltonian for the transition-metal $3d^8$ ions can be expressed as [33], $H = H_{ee}(B, C) + H_{SO}(\xi) + H_{Trees}(\alpha) + H_{CF}(D_q)$. In the above expression, H_{ee} (a function of the Racah parameters B and C) is associated with electron-electron repulsions which leads to the Russell-Saunders terms: the ground state ^3F (according to Hund rule), and the excited states ^3P, ^1G, ^1D, and ^1S [33]. The term H_{SO} represents the spin-orbit (SO) coupling, depending on the parameter ξ (the spin-orbit coupling constant). On the other hand, H_{Trees} (function of the Trees parameter α), is a correction term originating from a two-body orbit–orbit polarization interaction. The electron-electron interaction as in H_{ee} is a modification of an electronic cloud and hence

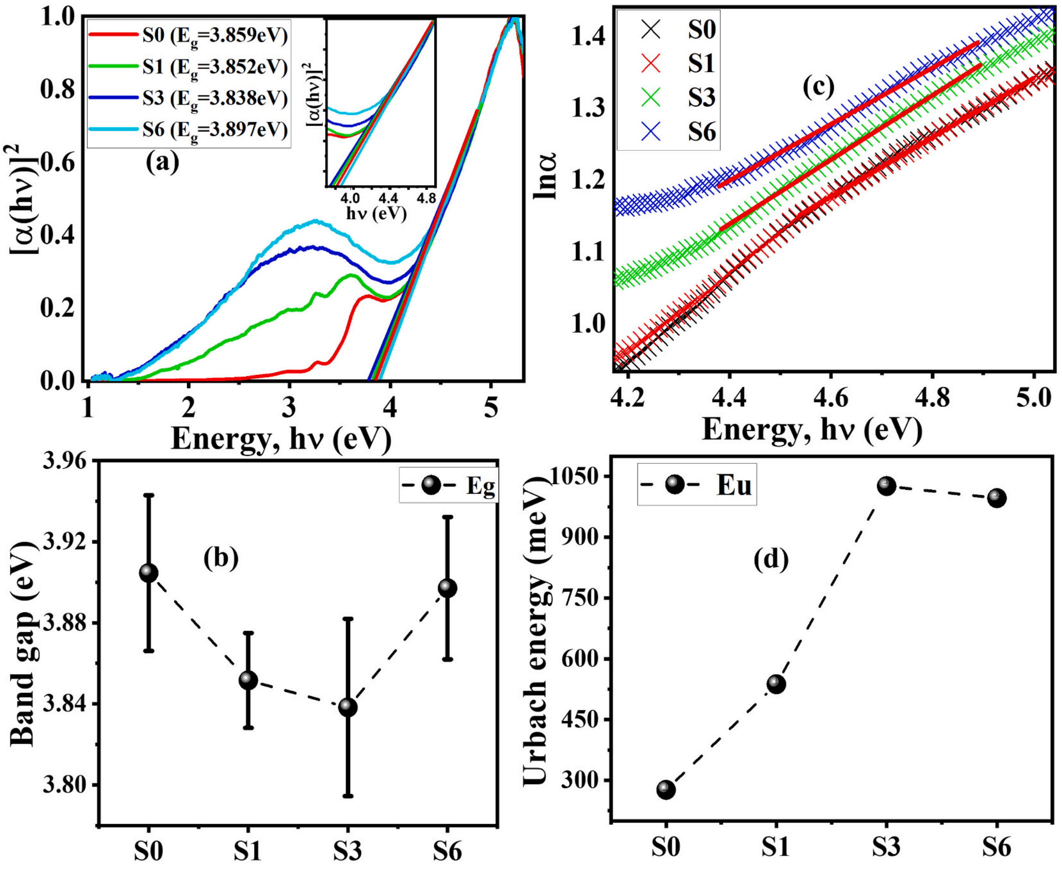

Fig. 7. (a) Tauc plots of Li doped NiO samples revealing changes in the direct band gap, (b) Variation of the E_g with substitution, (c) Linear fitting plots for E_u calculation (d) Variation of E_u with substitution.

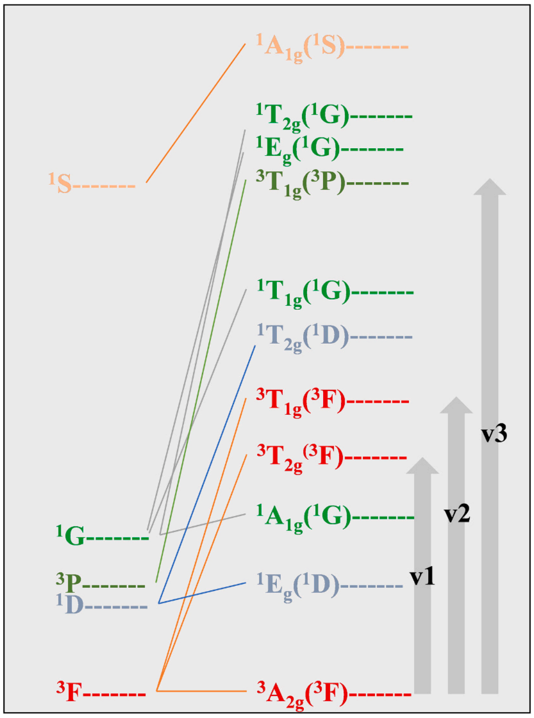

Fig. 8. Tanabe-Sugano diagram of a d^8 octahedral for Ni^{2+} along with the allowed transitions [33–35].

also associated with an orbit–orbit polarization. Hence H_{ee} and H_{SO} are often a result of a single change in the electronic cloud distribution. The $H_{CF}(D_q)$ component is dependent on D_q (a CF strength parameter) [33].

In an octahedral CF for a d^8-ion, Russell-Saunders energy levels split according to the strength of the octahedral ligand field. Note that the ^3F energy level splits into $^3T_{1g}$, $^3T_{2g}$, and $^3A_{2g}$ energy levels [31,33]. Similarly, the ^1D energy level will split into ^1E_g and $^1T_{2g}$ energy levels while the ^3P energy level will give $^1T_{1g}$, and ^1S term will give $^1A_{1g}$. The above splitting can be represented by the Tanabe-Sugano diagram [Fig. 8] for an extremely strong octahedral CF. Without any CF the energy levels are represented on the left-hand side of the diagram in the order $^3F < {}^1D < {}^3P < {}^1G < {}^1S$. In the strong octahedral CF, the energy levels are arranged in order $^3A_{2g}$ (^3F) < ^1E_g (^1D) < $^1A_{1g}$ (^1G) < $^3T_{2g}$ (^3F) < $^3T_{1g}$ (^3F) < $^1T_{2g}$ (^1D) < $^1T_{1g}$ (^1G) < $^3T_{1g}$ (^3P) < ^1E_g (^1G) < $^1T_{2g}$ (^1G) < $^1A_{1g}$ (^1S) [31,33,34]. Note that, all possible electronic transitions are not quantum-mechanically allowed [33,34]. The allowed transitions are defined by two rules: the spin selection rule and the Laporte rule [33,34]. According to the spin selection rule, transitions with unchanged total spin quantum number S (spin multiplicity) are allowed. On the other hand, the Laporte rule allows transitions with a change of parity ($g \Leftrightarrow u$). As a consequence of the above two rules only three electronic transitions ($S = 1 \Leftrightarrow S = 1$) can be expected from $^3A_{2g}(^3F)$ (i.e. the ground state) to $^3T_{2g}(^3F)$, $^3T_{1g}(^3F)$, and $^3T_{1g}(^3P)$, which belong to energies below the bandgap [33–35]. These three energy transitions are labeled as v_1, v_2, and v_3 respectively in Fig. 8 [11].

As discussed, Li^+ incorporation introduced Ni^{3+}, O_v, and Li_i. Such modifications in the lattice created disorder and defect states. Generally, disorder introduces modifications to the conduction band (CB) and valence band (VB) edges. Such modifications appear as band tails and are generally exponential in nature [23]: $\alpha = \alpha_0 . exp(h\nu/E_u)$, where, $h\nu$ represents the photon energy. Here, the term E_u represents an energy stored as a disorder in the lattice, known as Urbach energy. E_u was calculated from the slope of $\ln(\alpha)$ versus $h\nu$ plot [Fig. 7 (c)]. E_u increased from S0 (0.276 eV) to S1 (0.537 eV) to S3 (1.026 eV) and thereafter slightly reduced for S6 (0.996 eV) [Fig. 7 (d)] [11,12]. Hence, with Li^+ incorporation along with the increase of lattice strain, the lattice disorder also increased.

Hence, from the electronic properties study, it was observed that with Li^+ incorporation, the lattice got strained and disordered hinting at modifications in the electronic clouds of the atoms and thereby changes in the bond lengths. Such changes should affect lattice vibrations, transport properties, and charge storage properties.

3.5. Lattice vibration studies (Raman spectroscopy)

The room temperature Raman spectra [Fig. 9 (a)] of the synthesized nanostructures revealed prominent broad features at 400 and 530 cm^{-1}.

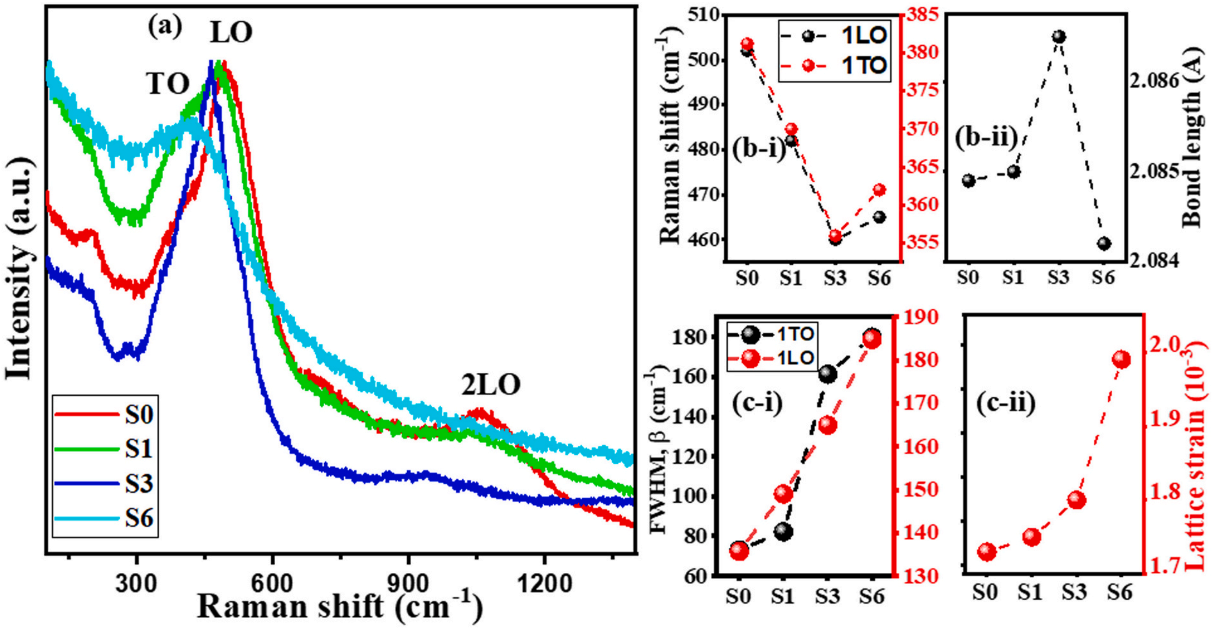

Fig. 9. (a) Raman spectra of Li doped NiO sample revealing modifications and shifts of the phonon modes, (b–i, ii) a close match of the nature of variance of the Raman shift and the bond length with doping, (c–i, ii) a close match of the increasing FWHM of 1P(LO) and 1P(TO) phonon modes and the lattice strain with substitution.

These corresponded to the 1P(TO) and 1P(LO) vibrational modes of the NiO lattice, respectively. Some additional weak features were also observed at 1090 cm^{-1} that were assigned to a two-phonon 2P(2LO) vibrational mode of NiO [13,23,36].

Due to Li^+ doping in the NiO lattice, the notable changes can be linked with the changes in the effective mass, bond strength (i.e. bond length), vacancies, and electrostatic interaction between ions. The mass of the dopant Li (~ 6.94 u) is much lighter than Ni (58.69 u). As phonon frequency is directly related to the square root of the bond strength and inversely to the square root of the effective masses of the vibrating atoms, such changes are most likely to affect the phonon modes in terms of frequency and intensity for the doped samples. Moreover, the valence state of dopant Li^+ is lesser than the host Ni^{2+}. Hence, one can expect more O_v in the doped lattice than the undoped pure NiO.

The 1P(LO) mode is purely due to an O—O planar vibration in the (111) plane, while, the 1P(TO) mode arises due to O—O transverse vibrations perpendicular to the (111) plane. Hence, both 1P(TO) and 1P (LO) are correlated to the O—O vibrations. Li^+ doping is expected to modify the oxygen lattice, thereby affecting these modes. Moreover, the lesser effective mass due to Li^+ substitution is likely to modify the phonon frequency to higher wavenumbers, i.e., a blue shift. There is a possibility that the Li^+-O^{2-} bond may be weaker than the Ni^{2+}-O^{2-} bond, which will be responsible for a redshift [13,23]. Experimentally the 1P(TO) mode has been observed to redshift from ~381 cm^{-1} (S0), to ~370 cm^{-1} (S1), to ~356 cm^{-1} (S3), while the 1P(LO) mode has redshifted from ~502 cm^{-1} (S0), to ~482 cm^{-1} (S1), to ~460 cm^{-1} (S3). For the S6 sample these modes were observed ~362 cm^{-1} (1P(TO)) and ~ 465 cm^{-1} (1P(LO)) [Fig. 9 (b)]. On the other hand, the FWHM of these modes increased continuously from ~77 cm^{-1} (S0) to ~86 cm^{-1} (S1), to ~149 cm^{-1} (S3), and ~ 188 cm^{-1} (S6) for the 1P(TO) mode and ~ 132 cm^{-1} (S0), to ~157 cm^{-1} (S1), to ~168 cm^{-1} (S3), and ~ 195 cm^{-1} (S6) for the 1P(LO) mode [Fig. 9 (c)] [13].

The redshift of these modes is possible due to two conditions: a weakened bond strength and an increase in the effective mass [23]. However, the effective mass decreased with Li doping thereby suggesting that the rate of weakening of the bond strength is far higher than the effect of decreasing rate of the effective mass of the vibrating atoms. This was observed more evidently from the increasing Ni^{2+}-O^{2-} bond length [Fig. 9 (b–ii)], which is an indication of the decreasing bond strength of these bonds [23,37]. The increasing FWHM was due to the increase of structural disorder in the lattice which is evident from the increasing strain [Fig. 9 (c-ii)] and Urbach energy from the UV–visible studies [37]. Such an increase in disorder was discussed in terms of increasing O_v in the lattice. Hence, the results of the Raman studies supported by the XRD and UV–visible studies, now can logically claim that O_v and O_i, i.e. in general oxygen species play an important role in the structure of the materials, thereby modifying their vibrational and electronic properties.

For the S6 sample, the amount of Li_i increased drastically to above 50%. These Li_i created a huge pressure in its vicinity, thereby compressing the local Ni—O bonds. Such a decrease in bond length has been observed in XRD studies. In such compressed lattice, the energy of vibration is generally increased and hence a blueshift of the concerned phonon is expected. The Raman spectrum of S6 did reveal a blue shift to ~465 cm^{-1}, confirming the increased lattice pressure due to Li incorporation which is consistent with the increase of strain from Williamson-Hall studies and disorder from Urbach energy studies.

A much broader and less intense 2LO mode was also observed ~1071.83 cm^{-1} for S0, which weakened and redshifted to lower wavenumber ~1040.79 cm^{-1} for S1 and ~ 936.21 cm^{-1} for S3. The feature vanished for S6. This feature can be attributed to the Ni—O stretching vibrations corresponding to the antiferromagnetic (AFM) strength of the lattice [23]. The reduction of structural symmetry due to increasing O_v content in the lattice near the Li^+ site, introduces modification of local Ni—O bond length and therefore affects the AFM ordering due to the disrupted lattice symmetry. On top of that, the advent of Li_i in S6, added to the degrading symmetry which was probably the reason behind the reduced AFM and thereby the vanishing of 2LO mode.

3.6. Cyclic Voltammetry

Among the different concentrations of the active materials, the CV spectra revealed a maximum enclosed area for the 4 mg sample implying the maximum C_s for this sample at 10 mV/s [Supplementary Fig. S1 (b)]. Therefore, 4 mg mass loading was used as a benchmark for further discussion. Oxidation and reduction peaks are related to the Faradaic reaction occurring on the electrode active surface in the CV spectra [3,8,38]:

$$\mathrm{NiO + OH^- \longrightarrow NiOOH + e^-}\ \text{(Oxidation, charging)}$$

$$\mathrm{NiOOH + H_2O_{ads} + e^- \longrightarrow \alpha - Ni(OH)_2 + OH^-}\ \text{(Reduction, discharging)}$$

$$\mathrm{\alpha - Ni(OH)_2 \longrightarrow NiO + H_2O}\ \text{(Dehydration in alkaline medium)}$$

Asymmetric redox peaks were observed at ~0.4 V (oxidation) and ~ 0.2 V (reduction), similar to reported values [11]. The asymmetricity was due to the kinetic irreversibility caused by interchange of electrons and ions during redox reactions.

C_s was calculated from the CV spectra [2,38]: $C_s = (\int idt)/(\Delta V \times m \times \vartheta)$. Here, $\int idt$ is the enclosed area under the curve, representing the total stored charge, ΔV is operating potential window, ϑ is scan rate, and m is mass deposited. The energy density (E) is the energy stored per unit mass, and is defined by [2]: $E = \frac{1}{2}C_s\Delta V^2$. On the introduction of Li^+ in a NiO lattice, the electronic structure, conductivity, and hence the electrochemical behavior was modified, thereby modifying the CV profiles [Fig. 10 (a), Supplementary Fig. S9]. Hence, the redox peak positions and the enclosed areas for a specific ϑ were different from sample to sample. From XRD and XPS it was concluded that Li^+ doping increased the Ni^{3+} percentage until S3. As a result of increased Ni^{3+} proportion, the amount of Ni^{3+}/Ni^{2+} redox couple increased, consequently improving the electrical conductivity. This increased electrical conductivity allowed faster electron transfer and therefore faster Faradaic reactions leading to higher pseudocapacitive storage. UV–vis absorption spectra revealed increased defect states inside the bandgap due to Li^+ incorporation, exposing more electroactive sites for redox reactions. Such increased defect states thereby facilitate the redox reactions. Hence, the increased enclosed surface area and peak potential shift can be correlated to such electronic changes leading to an improved C_s from 438.86 F g^{-1} in S0, to 465.08 F g^{-1} in S1, to 528.34 F g^{-1} in S3 at 5 mV/s [Fig. 10 (b)]. Thereby, the value of E increased from 21.94 J/g in S0, to 23.25 J/g in S1, to 26.41 J/g in S3 [Fig. 10 (c)]. For higher doping, i.e. for S6, XPS studies revealed a reduced Ni^{3+}/Ni^{2+} ratio. Hence, C_s reduced to 502.02 F g^{-1} for S6 as compared to 528.34 F g^{-1} in S3 but is higher than 465.08 F g^{-1} in S1. Similarly, E was lower (25.10 J/g) than S3 but higher than S1.

The charge storage capacity of all the electrodes can be attributed to two factors. Firstly, significant increase in the redox properties, and secondly, the amount of porosity of the materials [2]. While redox properties are an internal perspective and comes from changes in oxidation states of ions of the materials, the porosity depends on factors like agglomeration or networking of the nanoparticles. To understand how the surface area and other factors related to the agglomeration are affected by Li doping, N_2 adsorption–desorption (BET) measurements were carried out for all samples [Supplementary Fig. S10] [8]. The BET results revealed a nominal increase in specific surface area from 0.625 m^2g^{-1} (S0) to 0.68 m^2g^{-1} (S1) and thereafter drastically increased to 4.968 m^2g^{-1} (S3) [10], followed by a reduction to 1.134 m^2g^{-1} (S6) [10]. The pore diameter, nominally increased from 4.0 nm (S0) to 4.1 nm (S1) [10], thereafter revealed a continuous reduction to 3.35 nm (S3) and 2.47 nm (S6) [10]. The total pore volume revealed a continuous increase from 6.22×10^{-4} cm^3/g (S0) to 6.88×10^{-4} cm^3/g (S1), to

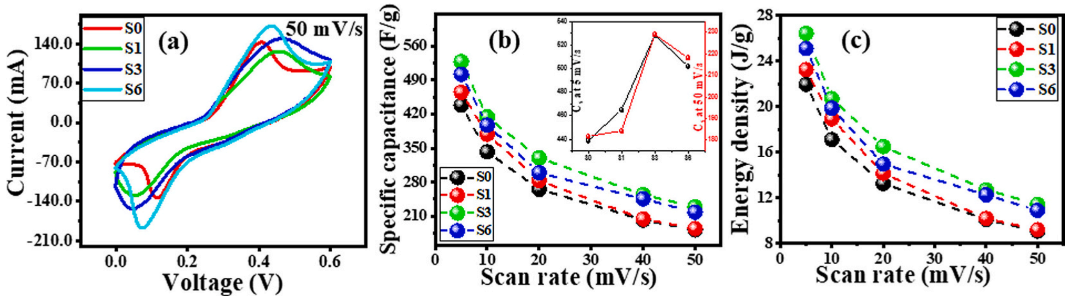

Fig. 10. (a) CV spectra for all samples at the same scan rate (50 mV/s), revealing increasing charge transfer and hence specific capacitance until S3 followed by a drop in S6, (b, c) reduction of specific capacitance and energy density with increasing scan rate for different samples respectively, note that the inset of (b) revealed of specific capacitance for two different scan rates (5 mV/s and 50 mV/s)".

Table 1
BET specific surface area, pore volume, and average pore diameter of the pristine and modified samples derived from N₂ adsorption–desorption isotherms.

Sample	BET surface area (m^2/g)	Avg. Pore diameter (nm)	Total pore volume (cm^3/g)
S0	0.625	4.0	6.22×10^{-4}
S1	0.68	4.1	6.88×10^{-4}
S3	4.968	3.35	4.17×10^{-3}
S6	1.134	2.47	2.0×10^{-3}

4.17×10^{-3} cm^3/g (S3), and then a reduction to 2.0×10^{-3} cm^3/g (S6) [Table 1] [10]. The continuous increase of surface area and pore volume from S0 until S3 should improve the electrolyte accessibility and thereby enhance electrochemical double-layer capacitance. Note that, from CV studies, a similar enhancement of the electrochemical performance was observed until S3 followed by a reduction in performance in S6. However, such a correlation between surface area/pore volume with the electrochemical performance may not be the entire story. Hence, the electrochemically active surface area was estimated using the Randles-Sevcik equation.

Randles-Sevcik equation for a supercapacitor defines the peak current (I_p) as: $I_p = (2.69 \times 10^3)n^{3/2}AD^{1/2}C\vartheta^{1/2}$ [2,10,39]. Here, n is the number of electrons transferred, A is the electrode surface area, D is the diffusion coefficient of the electroactive species, and C is the concentration of the redox species. The value of peak potential is given according to the relation [2,39]: $E_P = E^0 + \left(\frac{0.78RT}{\alpha nF}\right)\ln\vartheta$. Here, E^0 is the standard redox potential, α *is* charge transfer coefficient ($0 < \alpha < 1$), and R, T, F are universal constants. From the CV curves at different scan rates in 0–0.1 V potential window [Fig. 11 (a), Supplementary Fig. S11], C_{dl} values were calculated using slope value of $(j_a - j_c)/2$ and ϑ [Fig. 11 (b)], where j_a and j_c are anodic and cathodic current at a fixed potential (1.08 V RHE vs V). The C_{dl} values were found to be 0.103 mF-cm^{-2} for S0, 0.962 mF-cm^{-2} for S3, and 0.362 mF-cm^{-2} for S6. This resulted in an effective surface area from 2.576 cm^2 in S0, to 25.002 cm^2 in S3, and 9.039 cm^2 in S6 [Fig. 11 (c)]. This approach enabled differentiation between changes arising from increased electrochemically active sites and those originating from variations in physical surface area. The calculated ECSA values demonstrate a substantial increase in electrochemically accessible active sites for Li-doped samples, particularly S3.

The general form of the Randles-Sevcik eq. can be written in a form $I_p = a\vartheta^b$. The dimensionless value b predicts the expected charge storage mechanism; b is between 0 and 0.5 for battery materials, between 0.8 and 1.0 for capacitors, and mean b-values of 0.5–0.8, for supercapacitors [2]. The Randles-Sevcik eq. can be rewritten in the logarithmic form as [2]: $log(I_{ap}) = log(a) + b\, log(\vartheta)$. This provides a better understanding of the energy storage mechanism, by studying the influence of the scan rate on peak current [Fig. 12 (a), Supplementary Fig. S11]. The slope of the $log(I_{ap})$ vs $log(\vartheta)$ plots provided the b value. The b value decreased from ~0.769 in S0 to 0.703 in S1 and 0.659 in S3 and thereafter increased to 0.788 in S6 [Fig. 12 (b), Supplementary Fig. S12]. These values of b indicate a super-capacitive nature of electrodes that stores charge by both surface adsorption and diffusion mechanisms. These high b-values hinted towards a better performance at high scan rates because capacitive processes respond more quickly to voltage changes than diffusion-limited ones. Hence, the contribution of the capacitive and diffusion-controlled charge stored was obtained using Dunn's method at a fixed potential [2]: $I_p(\vartheta) = k_1\vartheta + k_2\vartheta^{1/2}$, where $k_1\vartheta$ and $k_2\vartheta^{1/2}$ are current contributions from the surface adsorption and diffusion-controlled processes, respectively. The contributions of capacitive and diffusion charge storage processes in the scan rate range of 5 to 50 mV/s were revealed in Fig. 12 (c) [supplementary Fig. S13]. At a scan rate of 5 mV/

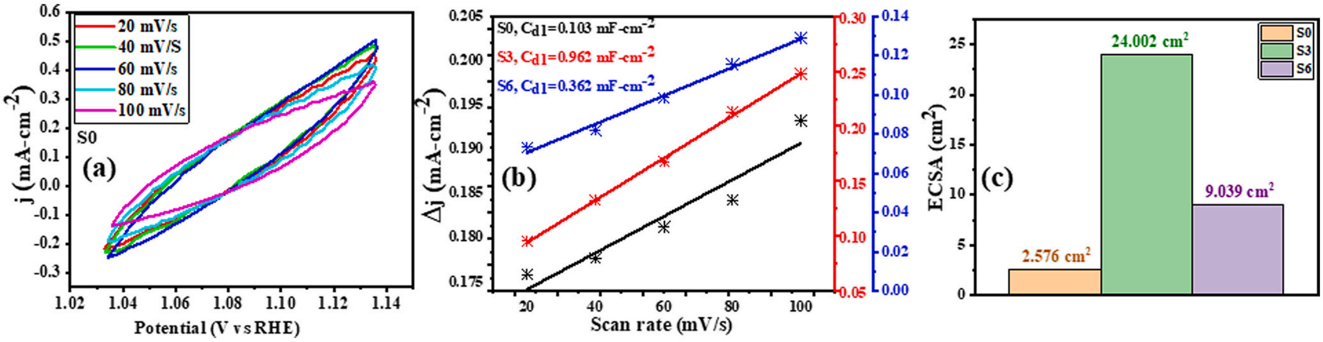

Fig. 11. (a) Cyclic voltammetry (CV) curves of the pure NiO electrode recorded at different scan rates (20–100 mV/s) within the window 1.02–1.14 V (RHE vs, V), (b) Linear fitting of the capacitive current density ($\Delta j = j_a - j_c$) as a function of scan rate for different samples, used to estimate the double-layer capacitance (C_{dl}) from the slope, (c) Comparison of electrochemical surface area (ECSA) values calculated from C_{dl} for S0, S3, and S6, showing a pronounced increase in electrochemically accessible active sites upon Li doping, particularly for S3.

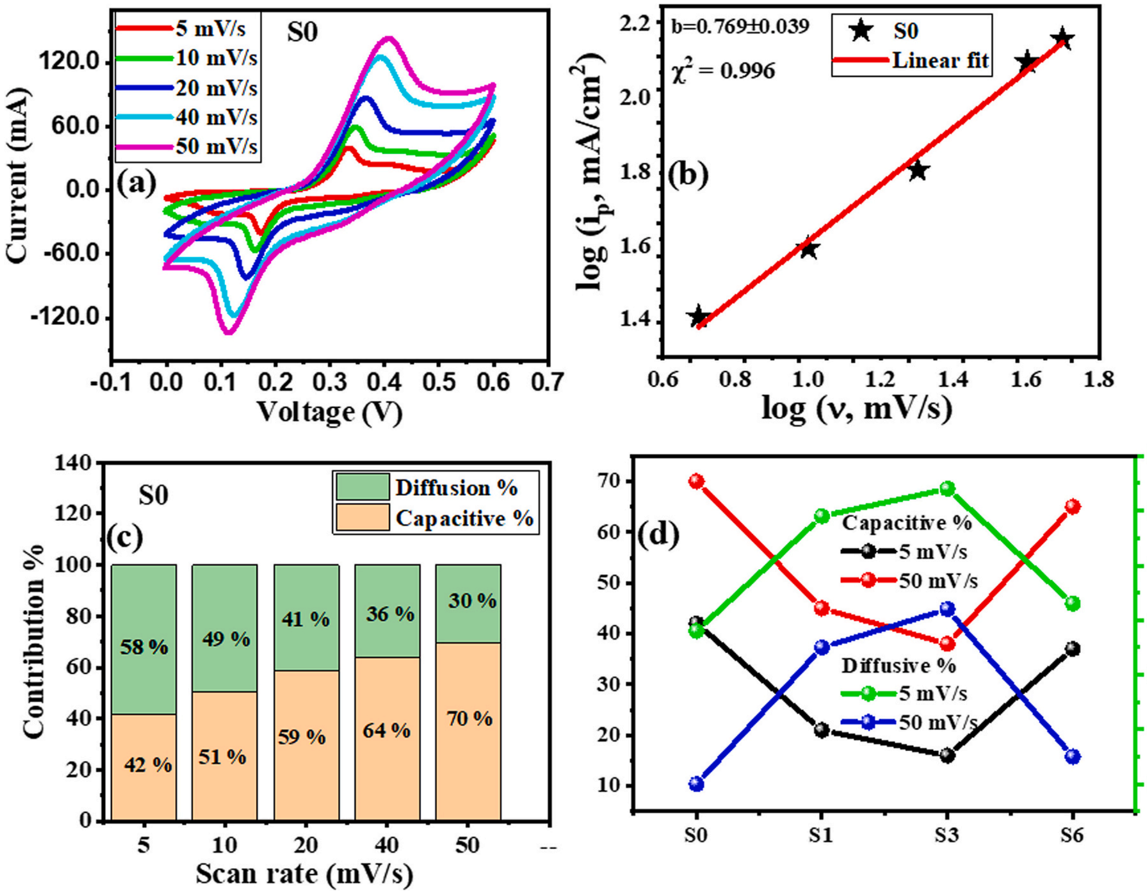

Fig. 12. (a) Cyclic voltammetry (CV) curves of the S0 electrode recorded at different scan rates (5–50 mV/s), showing the evolution of current response with increasing scan rate, (b) Power-law fitting of peak current as a function of scan rate (log i vs. log v) for S0, yielding a b-value of 0.769 ± 0.039, indicative of mixed surface-controlled and diffusion-controlled pseudocapacitive charge storage, (c) Relative contributions of capacitive (surface-controlled) and diffusion-controlled charge storage for S0 at different scan rates, obtained using Dunn's method, and (d) Variation of capacitive and diffusion-controlled contributions across different samples (S0–S6) at low (5 mV/s) and high (50 mV/s) scan rates, highlighting the evolution of charge storage mechanisms with Li doping.

s, the ratios of the capacitive to diffusive charge storage were 42:58 (S0), 21:79 (S1), 16:84 (S3), and 37:63 (S6). At a lower scan rate, ionic diffusion into deeper active sites becomes more possible, ensuring full redox kinetics due to more amount of time available, which is absent at higher scan rates. This enables the increasing capacitive contribution in the samples. An analysis was hence performed to find the percentage contribution of the capacitive component with different scan rates for all the samples. It was found that even for high scan rates, the capacitive contributions for S1 and S3 were less than 50%, whereas, for S0 and S6 [Fig. 12 (d)] these contributions were much higher, which may involve the contribution of pores and surfaces at higher scan rates for these samples. Hence, diffusion vs capacitive contributions from C*V* responses showed increasing pseudocapacitive fractions with Li-doping, particularly in S3, consistent with enhanced Faradaic charge storage rather than mere increments of surface area.

Hence, from this analysis some important factors can be established: a) the materials are super capacitive in nature, b) the major contribution of capacitance comes from the diffusive charge storage properties at lower scan rates for all samples, c) there is a possibility of capacitive increment in S0 and S6 samples at higher frequencies but for S1 and S3 contribution is mainly from diffusive property.

The GCD behavior of the S0 and Li^+-doped NiO electrodes was systematically investigated in the potential window of 0.0–0.4 V at various current densities to interpret their capacitive performance [Fig. 13(a–b), Supplementary Fig. S14]. All GCD curves exhibited a distinct quasi-triangular shape with characteristic plateaus, showing the coexistence of electric double-layer capacitance (EDLC) and Faradaic redox processes. The asymmetric nature of the GCD profiles, particularly at lower current densities, suggested irreversibility of the Li^+-assisted redox reactions. As the applied current density increased from 1.5 A g^{-1} to 20 A g^{-1} [Fig. 13 (a)], a progressive reduction in the discharge time was observed. This is consistent with the redox kinetics of the material related to the ion diffusion and electron transport properties at high scan rates.

Comparative GCD profiles at 1.5 A g^{-1} for different doping levels [Fig. 13 (b)] revealed a significant enhancement in the discharge duration upon Li^+ incorporation. This demonstrated its pivotal role in improving the electrochemical kinetics and charge storage capability. Quantitative analysis of the GCD curves using the relation [2]: $C_s = (I\ \Delta t)/(m\ \Delta V)$, confirmed a substantial improvement in the C_s with Li^+ doping. The S0 sample exhibited a C_s of 511.54 F g^{-1} (energy density, E = 11.36 J/g), which increased to 553.33 F g^{-1} (E = 12.26 J/g) for S1. A remarkable enhancement was observed for the optimally doped sample S3, reaching 888.15 F g^{-1} (E = 19 J/g), corresponding to a ~ 73.6% increase over S0. For the highest doping level (S6), the C_s and E values slightly decreased to 789.47 F g^{-1} and 17.54 J/g, respectively, which, although lower than S3, remained superior to both S0 and S1. This performance trend was consistent across the full current density range [Fig. 13 (c, c-i, and d)], where S3 consistently outperformed other compositions, suggesting an optimal substitutional Li^+ concentration for maximizing electroactive sites while avoiding excessive lattice distortion or agglomeration that might have hindered charge transfer.

Note that there is a notable discrepancy between capacitance values obtained from CV and GCD measurements. This discrepancy is an

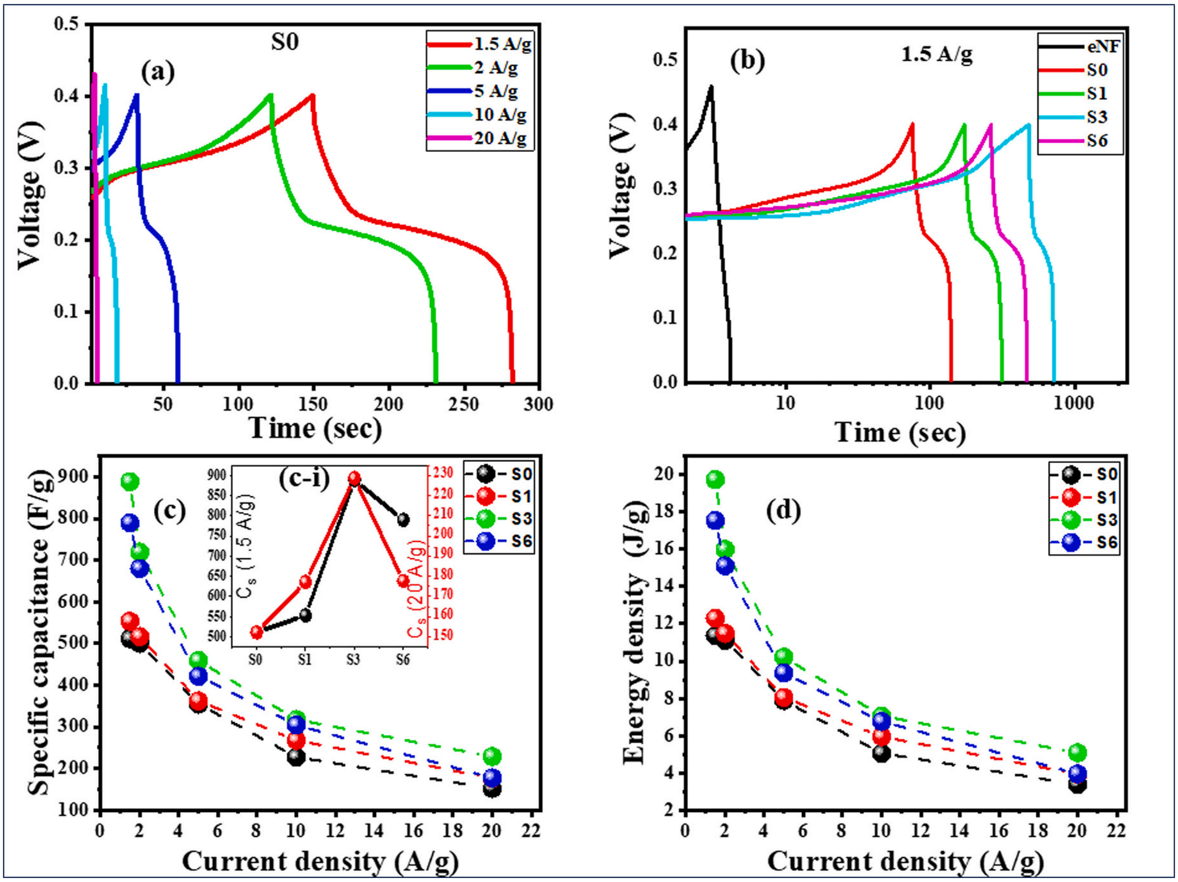

Fig. 13. (a) GCD spectra for pure NiO at different current density revealing non triangular nature thereby confirming a pseudocapacitive nature, (b) GCD spectra for all samples at the same scan rate (1.5 A/g) revealing a similar pseudocapacitive nature, (c, d) decreasing specific capacitance and energy density with increasing current density in different samples, respectively, and (c-i) increasing specific capacitance with doping until S3 followed by a decrement in S6 for both 1.5 A/g and 20 A/g current densities.

intrinsic property of pseudocapacitive electrodes and arises from the different time scales and charge-storage mechanisms probed in these two techniques. CV, performed under a linear potential sweep, predominantly captures fast surface-controlled processes and is excellent for analyzing performance at high scan rate [2]. However, for finite slower scan rates diffusion-limited bulk redox reactions are dominant. Internal resistance (IR) losses also affect CV strongly because both current and effective voltage vary continuously during the sweep. Hence, CV is used primarily to assess redox behavior, kinetics, stability, and operating potential windows [8].

On the other hand, a constant current is applied in GCD measurements [2], which allows sufficient time for deep ion diffusion [deeper penetration (diffusion depth, L_{GCD} $\left(\propto\sqrt{Dt}\right) > L_{CV}$] and full utilisation of bulk electroactive sites [2]. Therefore, GCD provides a more accurate quantitative measure of charge storage [2]. Generally, this yields higher capacitance values. Note that the capacitive values from GCD measurements were calculated using [2]: $C_{GCD} = (I\ \Delta t)/\ (m\ \Delta V)$, where Δt is usually much larger than $\Delta V/\upsilon$ in the capacitance expression for CV measurements [2]: $C_{CV} = (\int idt)/(\Delta V \times m \times \vartheta)$. This is the reason behind $Q_{GCD} > Q_{CV} \Leftrightarrow C_{GCD} > C_{CV}$. Note that accepting high scan rates in the CV measurement may be somewhat similar to high current measurements in GCD, a comparison may be done for all the samples. It was observed for a faster process (high scan rate/high current), the discrepancies of the value of capacitance for both CV/GCD measurements is minimal in all the samples. However, the discripencies becomes prominent for slower processes (low scan rate/high current). This further proves the charge storage properties are dependent on two different types of mechanisms, surface-controlled and diffusion-related properties, where diffusion plays an important role and is more visible at slow scan rate processes. Also to be noted is that the CV–GCD discrepancy increased with Li doping. It is to be remembered that Li^{+} doping increased the Ni^{3+} percentage until S3, increasing the Ni^{3+}/Ni^{2+} redox couples. Li-doping also introduced defects like O_v, Li_i and $Ni^{2+} \rightarrow Ni^{3+}$, generating lattice strain. These modifications are also responsible for modification in the electrical conductivity, which further allow faster electron transfer and therefore faster Faradaic reactions leading to higher supercapacitive storage. In this work, the CV–GCD discrepancy increased from $\sim$100 F g^{-1} for pristine NiO to $\sim$300 F g^{-1} for the Li-doped S3 sample [10]. Hence, a major contribution of the bulk-dominated storage mechanisms can be expected, overshadowing the surface effects. This explains the enhanced capacitance observed in the doped samples. Note that accepting high scan rates in the CV measurement may be somewhat similar to high current measurements in GCD, a comparison may be done for all the samples. It was observed for a faster process (high scan rate/high current), the discrepancies of the value of capacitance for both CV/GCD measurements is minimal in all the samples. However, the discrepancies become prominent for slower processes (low scan rate/high current) [Fig. 14]. This further proves the charge storage properties are dependent on two different types of mechanisms, surface-controlled and diffusion-related properties, where diffusion plays an important role and is more visible at slow scan rate processes.

For statistical validation (mean ± SD), over three independent CV and GCD measurements are provided [Supplementary Fig. S15]. The results are reported with relatively small standard deviations observed for both CV and GCD measurements, which confirmed good experimental reproducibility and data consistency. This statistical validation

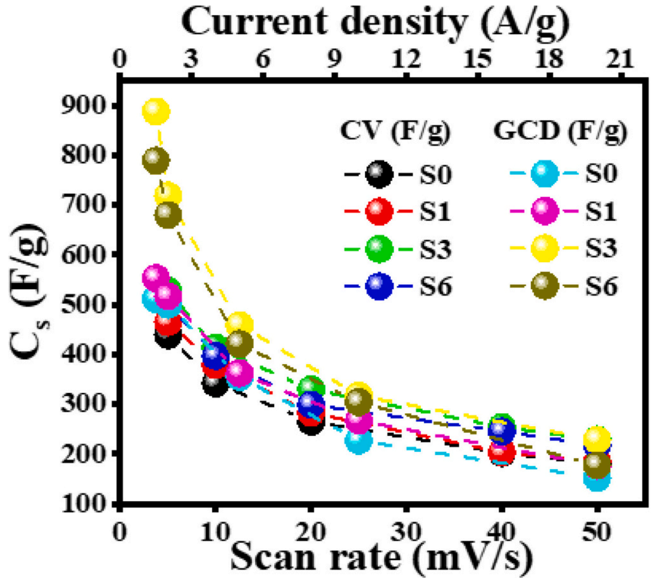

Fig. 14. Variation of specific capacitance of samples S0, S1, S3, and S6 as a function of scan rate (mV/s) obtained from CV and as a function of current density (A/g) obtained from GCD.

supported that the observed performance enhancement, as well as the CV–GCD discrepancy, arised from intrinsic electrochemical behavior rather than random experimental error or measurement uncertainty.

Hence, this study on Li-doped NiO revealed a strong correlation between structural modifications, optical properties, electrical performance, and electrochemical properties. With Li^+ incorporation, the strain and disorder in the lattice increased. It was observed that the tendency of Li^+ to occupy the interstitial positions increased with increasing Li content. In S1 and S3, Li^+ mostly substituted Ni^{2+}, thereby creating Ni^{3+} and oxygen defect species. For S6, approximately 50% of added Li^+ was interstitial. As a result, the Ni^{3+}/Ni^{2+} ratios and oxygen defect species were proportionately altered, thereby modifying the ligand field, electronic cloud distributions, lattice vibrations, transport properties, and thereby electrochemical properties. Hence, this work is just not about a substitution of Li^+ in NiO lattice but a guideline on how the nature of this substitution can affect the pseudocapacitive charge storage properties of an important material like NiO.

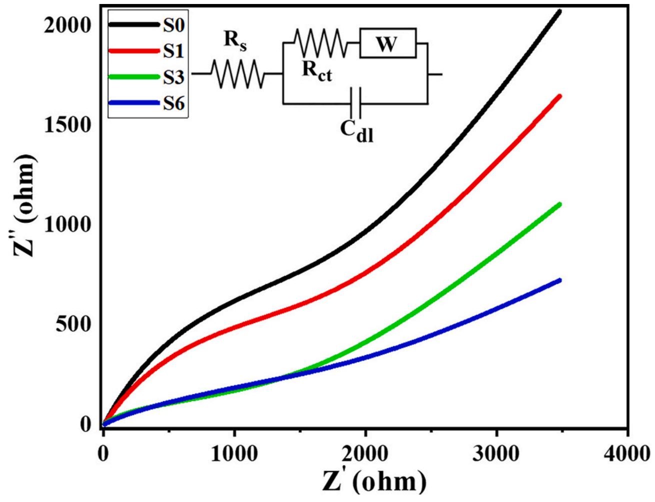

Fig. 15. Electrochemical impedance spectra for all samples along with the proposed equivalent circuit that is capable of fitting the spectra.

3.7. Impedance studies

EIS was carried out at the equilibrium potential (0 V) in 1 M KOH and shown in Fig. 15. The Nyquist spectra revealed a quasi-semicircle in the higher frequency range followed a low frequency, nearly-linear rise ascribable to Warburg function/impedance (Z_W). The quasi-semicircle feature was due to a charge transfer process taking place at the electrode/electrolyte interface. The diameter of the quasi-semicircle is equivalent to the charge transfer resistance (R_{ct}) [2]. The linear rise corresponds to the diffusion of the electrolyte ions from the bulk solution to the surface of the electrode [2]. The intersection of the EIS spectra with the real axis is the solution resistance (R_s) [2]. The classical Randles equivalent circuit [Fig. 15 (inset)] was employed to simulate the EIS spectra and the fitted values using the software ZVIEW are listed in Table 2. It was evident from the fitted values that there were negligible differences in Rs. With Li-doping, R_{ct} decreased drastically from 2.2 kΩ in S0 to 1.72 kΩ in S1 465 Ω in S3 and thereafter increased to 869 Ω in S6 [10,11]. A possible reason behind this reduction of R_{ct} is the formation of holes and oxygen defect species in the samples due to Li-incorporation. The C_{dl} value were found to continuously increase from 58.5 mF in S0, 72.7 mF in S1, 253 mF in S3 and 302 mF in S6. Note that from CV studies, for the non-Faradaic region, the purely capacitive C_{dl} values were found to be 0.103 mF-cm^{-2} for S0, 0.962 mF-cm^{-2} for S3, and 0.362 mF-cm^{-2} for S6. The C_{dl} values estimated from the slope of $(J_a - J_c)/2$ vs ϑ reflects a dynamic capacitive response during CV, whereas the values obtained from EIS corresponds to a near-equilibrium interfacial capacitance extracted under small-signal perturbation. Although both arise from the same electrochemical double layer, their numerical values are different due to differences in time scale, perturbation amplitude, and surface state contributions [10,11]. Note that R_{ct} decreased from S0 to S3 and thereafter increased for S6. A decrease in R_{ct} suggested that the kinetics of lithium-ion transfer at the interface have improved significantly due to doping. On the other hand, Z_W continuously increased with Li doping from 415 u-ohm for S0, to 519 u-ohm for S1, to 563 u-ohm for S3, and 1050 u-ohm for S6. This indicated a slow diffusion of Li^+ within the bulk material or to/from the electrode surface, despite a faster interfacial charge transfer. This could hypothetically occur if the doping introduces structural changes that, while being beneficial for charge transfer, somehow impede the long-range or bulk diffusion of lithium ions, leading to a higher Z_W even as the R_{ct} drops.

Based on the CV and EIS measurements, it was found that compared to pure NiO, 3% Li-doped NiO NPs have superior electrochemical activity. Since the S3 electrode exhibited the best overall pseudocapacitive performance, the electrode was further investigated for its stability and cycling capacity. Fig. 16, reveals the GCD profile of the S3 and S0 electrodes. The experiment was run for 1000 cycles in 6 M KOH electrolyte solution. The symmetric triangular-shaped GCD with a prominent plateau are characteristics of the supercapacitive behavior, which can be observed for the both the samples right from the first cycle till the 1000th cycle. The symmetric nature of the curves is also an indication that the electrode has suffered no fatal damage to its structure during this study. Moreover, the S3 electrode showed excellent capacitive retention of 92% at the end of the 1000th cycle [10], which confirms its remarkable cyclic stability.

In general, literature reports a high rate of current density (≥10 A/g) to facilitate testing of the electrode's robustness under high-power

Table 2
The fitted impedance parameters based on the proposed equivalent circuit.

Sample	R_s (ohm)	R_{ct} (ohm)	C_{dl}(mF)	Z_w/(ohm)	Chi^2
S0	5.25	2.2 k	58.5	415u	0.10075
S1	5.91	1.72 k	72.7	519u	0.08449
S3	9.89	465	253	563u	0.30862
S6	6.6	869	302	1.05 m	0.08285

operation. This enables probing high-rate mechanical and interfacial stability. Probing with high current density has been done by several groups [40– 45]. Comparatively low current densities are also reported in the literature [46,47]. At high current densities (high power), different failure modes may be encountered, such as electrode polarization, contact loss, mechanical strain, and fast surface reaction fatigue. Low current density cycling enables slow diffusion-limited degradation, phase changes, and electrolyte-induced dissolution or transformations. Consequently, retention or stability, measured at 10 A g^{-1}, can differ from that at lower current densities, depending on whether failure is dominated by high-current effects or by slow, diffusion- or bulk-related processes. At low current density, electrolyte ions have sufficient time to penetrate deeper into the electrode structure, enabling reversible redox reactions with minimal polarization and structural stress.

Keeping this point in mind, the stability was tested at both lower (5 A/g) and higher (10 A/g) current densities [Fig. 16] [10]. The stability result at 5 A/g yielded an 80% retention for S0, while for S6 it was ~99%. Whereas for 10 A/g, these values were 56% for S0 and 92% for S6. Hence, the changes in the retention values drastically changed from 80% to 56% in S0, while the change was only nominal, from 99% to 92% in S3 [10], indicating the better performance and stability of the Li-doped sample. Hence, Li-doping enables the lattice to have a better stable electrochemical robustness even if the cycling is performed with high current densities.

Hence, to summarize this work [Fig. 17], it should be mentioned that granular agglomerated NPs of Li-doped NiO revealed contraction of lattice parameters up to 3% doping followed by a marginal lattice expansion at 6% doping. The contraction can be attributed to $Ni^{2+} \rightarrow Ni^{3+}$ conversion resulting in a continuous increase of Ni^{3+}/Ni^{2+} ratio associated with simultaneous modifications in the O-lattice introducing O-defect species until 3%. An expansion in the lattice in the 6% sample may be due to the advent of Li_i. Minor reduction in direct bandgap (3.86 → 3.84 eV) was observed up to 3% doping followed by an increase at 6% doping. Lattice strain and disorder increased with increasing doping. Softening and broadening of LO/TO modes revealed weakening Ni—O bonds due to O-defects until 3%.

A strong correlation between the lattice modifications and capacitive behavior was observed with doping: S3 revealing maximum Cs = 528 F g^{-1} at 5 mV/s by CV and 888 F g^{-1} at 1.5 A g^{-1} by GCD. A ~ 74% enhancement was due to an increased Ni^{3+}/Ni^{2+} redox activity and defect-mediated conductivity as compared to S0. Excess Li_i in S6 reduced C_s. R_{ct} decreased by ~79%, before rising again for S6. The optimally doped electrode also exhibited outstanding cycling stability, retaining 92% capacitance after 1000 cycles.

However, the most important part of this work, is the segregation and decomposition of the different contribution of the materials in the supercapacitive performance, thereby concluding that the appropriate 3% substitution of Li^{+} leads to only one type of Li species which enables this material to obtain highest performance characteristics, which was not obtained for lower doped, higher doped, or undoped samples.

4. Conclusion

Li-doping of NiO seems to result in the replacement of Ni^{2+} by Ni^{3+} and Li + associated with the introduction of O-defects until 3% doping, thereby increasing the lattice strain and disorder. New modified bonds like Li^{+}-O^{2-}, Ni^{3+}-O^{2-}, Ni^{2+}-O_v, Li^{+}-O_v, etc. in place of Ni^{2+}-O^{2-} changes the ligand field of the lattice locally, bringing in modifications in the bond strength, thereby modifying the vibrational and electronic properties and hence improving the transport properties. The C_{dl} value were found to continuously increase from S0 to S6, from EIS studies, but from non-Faradaic CV studies, a particular trend was not obtained. This

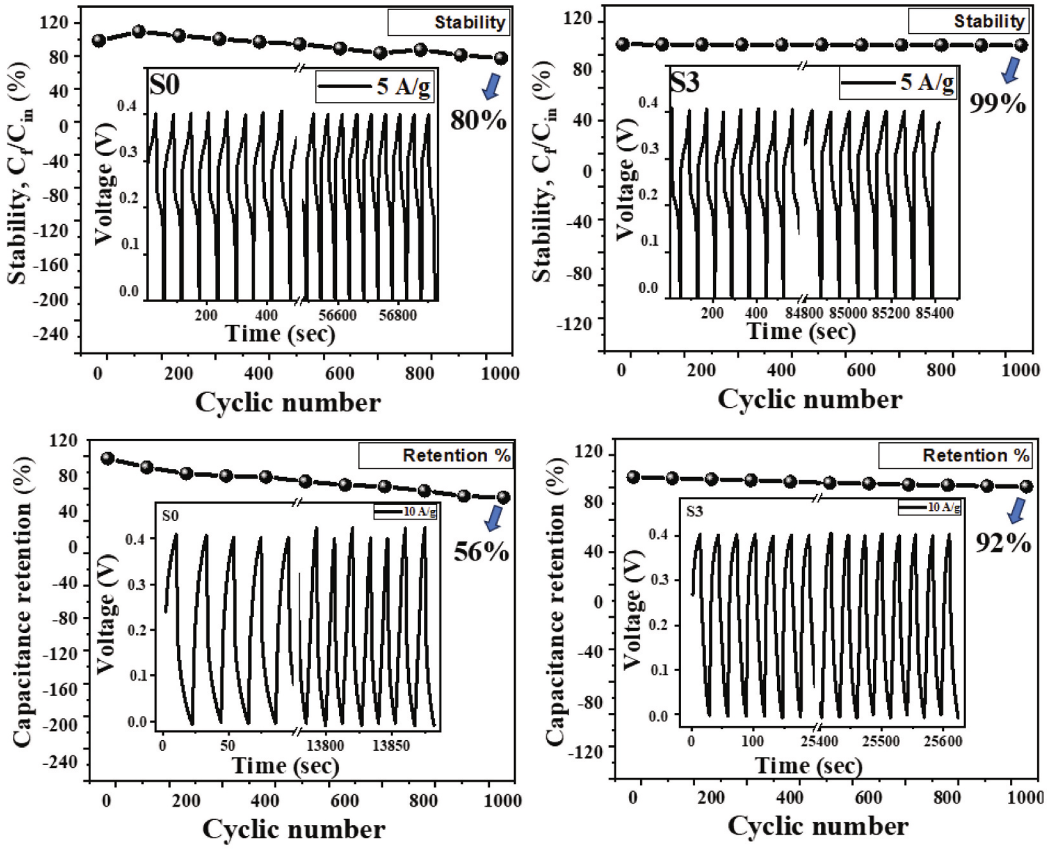

Fig. 16. Experimenting of the cyclic stability of the pure and S3 samples for 1000 GCD cycles at 5 A/g with a retention of 80% in pure and 99% in S3 sample and at 10 A/g with a retention of 56% in pure and 92% in S3 sample.

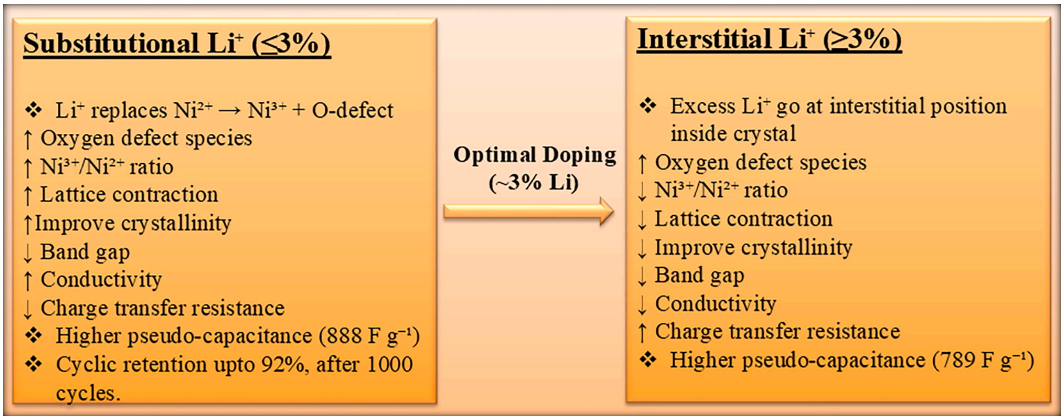

Fig. 17. Comparison of substitutional and interstitial Li^+-ion in the tuning of Oxygen defect species and Ni^{3+} Content for High-Performance NiO Supercapacitors.

difference arises from the differences in time scale, perturbation amplitude, and surface state contributions. For the optimally 3% doped sample, C_s increased by ~74%, while R_{ct} decreased by ~79%, resulting in an excellent retention of 99% at 5 A/g and 92% at 10 A/g after 1000 cycles, showing remarkable cyclic stability. On the other hand, an excess or shortage of Li^+ ion incorporation in NiO results in detrimental performance of the electrode.

CRediT authorship contribution statement

Poonam Singh: Writing – original draft, Visualization, Methodology, Investigation, Formal analysis, Data curation, Conceptualization. **P. Maneesha:** Writing – review & editing. **Manju Kumari:** Data curation. **Abdelkrim Mekki:** Data curation. **Khalil Harrabi:** Data curation. **Somaditya Sen:** Writing – review & editing, Validation, Supervision, Resources, Project administration.

Declaration of competing interest

The authors declare that they have no known competing financial interests or personal relationships that could have appeared to influence the work reported in this paper.

Acknowledgments

S. Sen would like to acknowledge the Department of Science and Technology (DST), Govt of India for providing the funds (DST/TDT/AMT/2017/200). The authors also acknowledge the Department of Science and Technology (DST), Govt. of India, for providing FIST funded Raman Spectrometer (Grant Number SR/FST/PSI-225/2016) at the Department of Physics, IIT Indore. P. Maneesha would like to thank the Ministry of Education, Government of India for the Prime Minister Research Fellowship (PMRF), Govt. of India. M. Kumari would like to thank UGC-SRF (211610074937) for providing fellowships. A. Mekki and K. Harrabi would like to thank KFUPM for providing funds for conducting research. P. Singh acknowledges the constant moral support of Rakhi Saha, Dilip Sasmal, Prashant Joshi and Garvit Shrivastava. Finally P. Singh would like to acknowledge the teaching assistantship provided by IIT Indore.

Appendix A. Supplementary data

Supplementary data to this article can be found online at https://doi.org/10.1016/j.jelechem.2026.119883.

Data availability

Data will be made available on request.

References

[1] J. Mitali, S. Dhinakaran, A.A. Mohamad, Energy storage systems: a review, Energy Storage and Saving 1 (3) (2022) 166–216.
[2] K.C. Seetha Lakshmi, Balaraman Vedhanarayanan, High-performance supercapacitors: a comprehensive review on paradigm shift of conventional energy storage devices, Batteries 9 (4) (2023) 202.
[3] Ranjit S. Kate, Suraj A. Khalate, Ramesh J. Deokate, Overview of nanostructured metal oxides and pure nickel oxide (NiO) electrodes for supercapacitors: a review, J. Alloys Compd. 734 (2018) 89–111.
[4] Kohei Matsubara, et al., Enhanced conductivity and gating effect of p-type Li-doped NiO nanowires, Nanoscale 6 (2) (2014) 688–692.
[5] Kingsley O. Egbo, et al., Efficient p-type doping of sputter-deposited NiO thin films with Li, ag, and cu acceptors, Phys. Rev. Mater. 4 (10) (2020) 104603.
[6] Wu Chia-Ching, Yang Cheng-Fu, Investigation of the properties of nanostructured Li-doped NiO films using the modified spray pyrolysis method, Nanoscale Res. Lett. 8 (2013) 1–5.
[7] Xiangbao Yuan, et al., Enhanced p-type conductivity of NiO x films with divalent cd ion doping for efficient inverted perovskite solar cells, ACS Appl. Mater. Interfaces 14 (15) (2022) 17434–17443.
[8] Rini Paulose, Raja Mohan, Vandana Parihar, Nanostructured nickel oxide and its electrochemical behaviour—a brief review, Nano-Struct. Nano-Objects 11 (2017) 102–111.
[9] Robert D. Shannon, Revised effective ionic radii and systematic studies of interatomic distances in halides and chalcogenides, Foundations of Crystallography 32 (5) (1976) 751–767.
[10] R. Ranjitha, et al., Rapid photocatalytic degradation of cationic organic dyes using Li-doped Ni/NiO nanocomposites and their electrochemical performance, New J. Chem. 45 (2) (2021) 796–809.
[11] Aarti S. Bhatt, et al., Optical and electrochemical applications of Li-doped NiO nanostructures synthesized via facile microwave technique, Materials 13 (13) (2020) 2961.
[12] Abdellatif Laib, et al., Effect of Li doping on the structural, linear and nonlinear optical properties of NiO thin films, Ferroelectrics 599 (1) (2022) 186–200.
[13] Xianglan Xu, et al., Engineering Ni3+ cations in NiO lattice at the atomic level by Li+ doping: the roles of Ni3+ and oxygen species for CO oxidation, ACS Catal. 8 (9) (2018) 8033–8045.
[14] J.Y. Zhang, et al., Electronic and transport properties of Li-doped NiO epitaxial thin films, J. Mater. Chem. C 6 (9) (2018) 2275–2282.
[15] Wei-Luen Jang, et al., Electrical properties of Li-doped NiO films, J. Eur. Ceram. Soc. 30 (2) (2010) 503–508.
[16] Titas Dutta, et al., Effect of Li doping in NiO thin films on its transparent and conducting properties and its application in heteroepitaxial pn junctions, J. Appl. Phys. 108 (2010) 8.
[17] U.S. Joshi, et al., Structure of NiO and Li-doped NiO single crystalline thin layers with atomically flat surface, Thin Solid Films 486 (1–2) (2005) 214–217.
[18] Suman Mandal, Krishnakumar S.R. Menon, Hole-states in Li doped NiO: doping dependence of Zhang-Rice spectral weight, Phys. Chem. Chem. Phys. 26 (43) (2024) 27735–27740.
[19] J. Van Elp, et al., Electronic structure of Li-doped NiO, Phys. Rev. B 45 (4) (1992) 1612.
[20] I. Sta, et al., Hydrogen sensing by sol–gel grown NiO and NiO: Li thin films, J. Alloys Compd. 626 (2015) 87–92.
[21] I.A. Garduño, et al., Optical and electrical properties of lithium doped nickel oxide films deposited by spray pyrolysis onto alumina substrates, J. Cryst. Growth 312 (22) (2010) 3276–3281.
[22] Hakim Moulki, et al., Improved electrochromic performances of NiO based thin films by lithium addition: from single layers to devices, Electrochim. Acta 74 (2012) 46–52.
[23] Prashant Kumar Mishra, et al., Electroluminescence, UV sensing, and pressure-induced conductance of Li^+/Al^{3+} modified NiO: theoretical/experimental insights, J. Mater. Res. 38 (9) (2023) 2550–2565.

[24] Anupama Bhankhar, et al., A comparative study of experimental and theoretical structural analysis of Lithium doped nickel oxide nanoparticles, ECS journal of solid state Sci. Technol. 12 (1) (2023) 013001.

[25] Ziyi Xiao, et al., Lithium doped nickel oxide nanocrystals with a tuned electronic structure for oxygen evolution reaction, Chem. Commun. 57 (49) (2021) 6070–6073.

[26] S. Gražulis, D. Chateigner, R.T. Downs, A.T. Yokochi, M. Quiros, L. Lutterotti, E. Manakova, J. Butkus, P. Moeck, A. Le Bail, Crystallography open database – an open-access collection of crystal structures, J. Appl. Crystallogr. 42 (2009) 726–729.

[27] Tithi Sen, et al., Enhanced electrochemical performance of NiO surfaces via selective Li+ doping, Phys. Chem. Chem. Phys. 26 (42) (2024) 27141–27151.

[28] Yan Li, et al., One-step synthesis of Li-doped NiO as high-performance anode material for lithium ion batteries, Ceram. Int. 42 (13) (2016) 14565–14572.

[29] Radostina Stoyanova, et al., Correlations between lithium local structure and electrochemistry of layered LiCo 1− 2x Ni x Mn x O 2 oxides: 7 Li MAS NMR and EPR studies, Phys. Chem. Chem. Phys. 16 (6) (2014) 2499–2507.

[30] Xiao Liang, et al., Tuning transition metal oxide–sulfur interactions for long life lithium sulfur batteries: the "goldilocks" principle, Adv. Energy Mater. 6 (6) (2016) 1501636.

[31] V. Helan, et al., Neem leaves mediated preparation of NiO nanoparticles and its magnetization, coercivity and antibacterial analysis, Results Phys. 6 (2016) 712–718.

[32] Imen Elhamdi, et al., Experimental and modeling study of ZnO: Ni nanoparticles for near-infrared light emitting diodes, RSC Adv. 12 (21) (2022) 13074–13086.

[33] M.G. Brik, et al., Spin-forbidden transitions in the spectra of transition metal ions and nephelauxetic effect, ECS J. Solid State Sci. Technol. 5 (1) (2015) R3067.

[34] Giancarlo Trimarchi, Zhi Wang, Alex Zunger, Polymorphous band structure model of gapping in the antiferromagnetic and paramagnetic phases of the Mott insulators MnO, FeO, CoO, and NiO, Phys. Rev. B 97 (3) (2018) 035107.

[35] Bärbel Fromme, electronic structure of MnO, CoO, and NiO, in: dd excitations in transition-metal oxides: a spin-polarized Electron energy-loss spectroscopy (SPEELS) Study, 2001, pp. 5–26.

[36] Ghadah M. Al-Senani, et al., One pot synthesis, surface, and magnetic properties of Ni–NiO@ C nanocomposites, Crystals 13 (10) (2023) 1497.

[37] J. Arunodaya, Trilochan Sahoo, Effect of Li doping on conductivity and band gap of nickel oxide thin film deposited by spin coating technique, Mater. Res. Express 7 (1) (2019) 016405.

[38] Nor Azmira Salleh, Soorathep Kheawhom, Ahmad Azmin Mohamad, Characterizations of nickel mesh and nickel foam current collectors for supercapacitor application, Arab. J. Chem. 13 (8) (2020) 6838–6846.

[39] Xiaoyan Hu, et al., Nickel foam and stainless-steel mesh as electrocatalysts for hydrogen evolution reaction, oxygen evolution reaction and overall water splitting in alkaline media, RSC Adv. 9 (54) (2019) 31563–31571.

[40] Bakar, Nor Atikah Abu, et al., The effect different of hydrochloric acid concentrations on the cleaning of Ni foam substrate: structural and morphological studies, Mater. Today Proc. 60 (2022) 1036–1041.

[41] Laifa Shen, et al., Mesoporous NiCo2O4 nanowire arrays grown on carbon textiles as binder-free flexible electrodes for energy storage, Adv. Funct. Mater. 24 (18) (2014) 2630–2637.

[42] Mingfei Shao, et al., Core–shell layered double hydroxide microspheres with tunable interior architecture for supercapacitors, Chem. Mater. 24 (6) (2012) 1192–1197.

[43] M. Manikandan, et al., Engineering NiO/g-C_3N_4 and NiO/rGO composites for dual applications in electrochemical water splitting and energy storage, Sci. Rep. 15 (1) (2025) 36708.

[44] Xu Zou, et al., Ultrafast surface modification of Ni3S2 nanosheet arrays with Ni-Mn bimetallic hydroxides for high-performance supercapacitors, Sci. Rep. 8 (1) (2018) 4478.

[45] Zhongli Hu, et al., Secondary Bonding Channel design induces intercalation Pseudocapacitance toward ultrahigh-capacity and high-rate organic electrodes, Adv. Mater. 33 (44) (2021) 2104039.

[46] Pankaj Kumar Sharma, et al., synergistic effect of Mo doping on the pseudocapacitive performance of Zn–V–O based TMOs for supercapacitor applications, Nanoscale Adv. 7 (23) (2025) 7638–7652.

[47] Yu Ma, et al., High energy density and extremely stable supercapacitors based on carbon aerogels with 100% capacitance retention up to 65,000 cycles, Proc. Natl. Acad. Sci. 118 (21) (2021) e2105610118.